國 立 交 通 大 學

加速器光源科技與應用碩士學位學程

碩 士 論 文

極紫外光微影之鉬矽多層膜鏡片與光罩反射率改善研究

Reflectance Improvement of Mo/Si Multilayer Mirrors and Masks for Extreme Ultra-Violet Lithography

研 究 生 ：劉芳宜　　Fang-Yi Liu

指導教授 ：黃遠東 教授　Prof. Yang-Tung Huang

許博淵 博士　Dr. Bor-Yuan Shew

中華民國 一〇一 年 一 月

極紫外光微影之鉬矽多層膜鏡片與光罩反射率改善研究

Reflectance Improvement of Mo/Si Multilayer Mirrors and Masks for Extreme Ultra-Violet Lithography

研 究 生 ：劉芳宜　　Student: Fang-Yi Liu

指導教授 ：黃遠東　　Advisor: Prof. Yang-Tung Huang

許博淵　　Dr. Bor-Yuan Shew

國立交通大學

加速器光源科技與應用碩士學位學程

碩 士 論 文

A Thesis

Submitted to Graduate Program for Science and Technology of Accelerator Light Source

College of Engineering

National Chiao Tung University

In Partial Fulfillment of the Requirements

For the Degree of Master

In

Graduate Program for Science and Technology of Accelerator Light Source

January 2012

Hsinchu, Taiwan, Republic of China

中華民國 一〇一 年 一 月

極紫外光微影之鉬矽多層膜鏡片與光罩反射率改善研究

研究生：劉芳宜　　指導教授：黃遠東 教授

許博淵 博士

國立交通大學

加速器光源科技與應用碩士學位學程

摘 要

本研究主要探討極紫外光微影之鉬矽多層結構之設計與特性。其四分之一波膜反射率可以藉由調整膜層厚度的最佳化程序達到較好效能，而於商業用的極紫外光微影系統其要求多層膜需具備高反射率效果及較好的穩定性。本研究以介面工程 (interface-engineered) 完成了在 13.5-nm 波長具有 72.62%反射率及 0.828 nm 半高全寬介面工程鉬矽(Mo/Si)多層膜結構之開發，此結構則包含被 boron carbide (B_4C) 與 ruthenium (Ru) 材料所分隔的鉬矽交錯層，Ru 和 B_4C 的屏障層 (barrier layer) 則被分別插入於鉬和矽 (Mo-on-Si) 及矽和鉬 (Si-on-Mo) 的介面中形成 54 對的 Ru/Mo/B_4C/Si 多層膜。與傳統的四分之一波膜相比，在 13.5-nm 波長大約有 4%的反射率改善，將 1.4 nm 厚的 Ru 的 0.2 nm 厚的 B_4C 插入鉬矽多層膜的介面可以達到此最佳反射率。另外，現今主要關注的議題之一是由於表面光子輻射所導致的光學式表面汙染將會減低光電元件的使用壽命；而從模擬結果看來最有希望成為覆蓋層 (capping layer) 的材料是 Ru。藉由將 Ru 覆蓋於介面工程鉬矽多層膜結構最上層可達到對極紫外光的氧化抵抗力，在經由極紫外光曝光環境的過程中這個結構能夠具有高反射率以及抗氧化力。

Reflectance Improvement of Mo/Si Multilayer Mirrors and Masks for Extreme Ultra-Violet Lithography

Student: Fang-Yi Liu Advisor: Prof. Yang-Tung Huang

Dr. Bor-Yuan Shew

Graduate Program for Science and Technology of Accelerator Light Source

National Chiao Tung University

ABSTRACT

In this study, the design and characteristics of Mo/Si multilayers for extreme ultra-violet (EUV) lithography have been investigated. The reflectance of the quarter-wavelength multilayers can be enhanced further by optimized procedures with which the layer thicknesses are varied for best performance. For commercial EUV lithographic systems multilayer mirrors and masks require with higher reflectance and better stability. Interface-engineered Mo/Si multilayers with 72.62% reflectance and a FWHM of 0.828 nm at 13.5-nm wavelength have been developed and simulated. The design was achieved with 54 pairs of Ru/Mo/B_4C/Si multilayer. This structure consist of alternating Mo and Si layers separated by thin boron carbide (B_4C) and ruthenium (Ru) layers. Ru barrier layer was inserted into a Mo-on-Si interface and B_4C barrier layer was inserted into a Si-on-Mo interface to improve the EUV reflective multilayer properties. About 4 % improvement of the reflectance at 13.5-nm wavelength compared to standard quarter-wave stacks can be acquired by the design. The best results according to simulation were obtained with 1.4-nm-thick Ru layers for the Mo-on-Si interfaces and 0.2-nm-thick B_4C layers for the Si-on-Mo interfaces. The contaminations of optical surfaces by photon irradiation in the presence shorten optics lifetime become one of the main concerns. From simulation results, the most promising candidate seems to be Ru. The improvement in oxidation resistance of EUV multilayers has been achieved with Ru -capped interface-engineered Mo/Si multilayers. This structure achieves high reflectance and the great oxidation resistance during the EUV exposure in a water-vapor (oxidized) environment. Based on simulation results, we calculated reflectance for the reflective multilayer mirrors in a EUVL procedure and concluded that Ru-capped Ru/Mo/B_4C/Si multilayers have a higher performance than quarter-wave Mo/Si multilayers. The simulation results clearly show reflectance improvement of our designed structure compared with standard Mo/Si multilayer structures.

誌謝

漫長的碩士生涯終於要結束了，想想過去兩年多在模擬上經歷了很多挫折，從不熟悉語言程式的門外漢到現在可以又驕傲又獨立的寫出一些有意義成果的 code。曾經無助、沮喪的想就此放棄，卻也一路上得到了很多人鼓勵和協助才能夠撐到這篇論文的誕生，就讓我利用這短短的篇幅獻上最深切的感謝。

指導教授黃遠東博士以平時對英文的要求督促我以英文完成本篇論文，且熟悉於人際關係的行為模式令人十分佩服，是我值得學習的典範。非常謝謝老師在實驗模擬上讓我有很大的空間自己探究、摸索以及之後次次詳細的論文修改，讓我在這兩年半的時間裡對於人事物有所成長。接著是對於 EUV 這個領域雖然不太了解，卻也能夠適時以其原本的聰明才智進而提點我的徐新峰學長, 努力不懈的研究精神讓人佩服，祝福你快點拿到博士學位找到心目中的工作。還要感謝能在碩士生涯遇見的蘇婷婷、程建瑋、張書維、邱霆宇、楊智翔、許茗舜的你們，感謝在我苦悶的課業生活上給予幫助及帶來歡笑和感動。還有實驗室的陳建華、劉宇修、謝宗謀、蘇倉賢和黃一平學長們與林政文、李承翰、蔡翼鍾、廖浚宏學弟們都很謝謝你們這些日子以來的鼓勵和幫助。

即使山上的風太大了，慢慢走還是會抵達的，一定可以走完最後一里路；這些日子過得好久好長，卻又在眨眼之間消逝，也許選擇了一條顛頗的道路，但不管多麼崎嶇還是能遇見終點的。最後的最後，我很愛也愛著我的家人，感謝你們的溫暖支持總是給予適時心靈幫助，謝謝！！

Contents

List of Tables

List of Figures

Chapter 1

Introduction

1.1 The Evolution of Lithography

The fast development in manufacturing technology of integrated circuits has followed the Moore's law for years; and the number of transistors on a chip has grown doubling on the average of every 18 months exponentially. The role of lithography has been more important not only because of the requirements for smaller feature sizes and tighter overlay, but also because of the increasing costs of lithography tools [1].

The fundamental relationship in lithographic imaging system is resolution which can be described

$$\text{Resolution} = k_1 \lambda / \text{NA} \tag{1.1}$$

where k_1 is constant, λ is the wavelength of the imaging radiation, and NA is the numerical aperture of the imaging system.

Therefore, when IC feature size shrank, the indusry used the expose source from g-line (436 nm), ultraviolet (365 nm), 248-nm KrF, to 193-nm ArF by excimer lasers in lithography technology [2]. In the 193-nm stage, even the multiple patterns where used to achieve the 22-nm pitch. Regardless of what method, high throughput and low cost of ownership must be satisfied [3], [4]. The following will list some methods for the next generation lithography (NGL), and several unique challenges also would be introduced.

Figure 1-1 shows the equipment of the imprint lithography. The pattern is created on a template made of glass. Then a template is pressed on the coating resist to transfer the pattern. Exposing with an ultraviolet light, let the photoresist react and form a pattern.

To reduce the linewidth, the 1X mask should be smaller; moreover, defects in the pattern must be below 10% of the width of the feature. And the resist should be with a lower viscosity for sufficient throughput. In addition, the production costs include the template life time and imprint material cannot be too high.

Electron beam lithography is a kind of maskless lithography, and Figure 1-2 shows the equipment set-up of e-beam lithography system [5]. Electron beam method is used to create patterns on a wafer directly and a smaller beam source could achieve a smaller line width. Maskless lithography eliminates the problems of mask lifetime and mask defect. Although there is no mask cost in direct-writing lithography, e-beam lithography need overcome the major challenge is the wafer throughput. Multiple-beam direct writing is developed for improving throughput, and the system combining with the resist sensitivity may provide a higher resolution. Besides, another problem in e-beam lithography is the inaccuracies on the wafer due to the charging effect.

One of the earliest and most important decisions made in the field of EUVL was the choice of the exposure wavelength. That influenced the design of the projection optics, set the peak reflectance and bandwidth of the multilayer reflective coatings, and had an impact on the performance of EUV materials. Figure 1-3 shows the equipment set-up of EUV lithography [6]. The wavelength in this region is shorter than other exposure sources in lithography, which wiil be absorbed in most materials, and thus all equipment should be enclosed in a high vacuum environment. Furthermore, to avoid EUV absorption, optics and mask in the system are reflective and defect-free by multilayer-coating mirrors, i.e., the quarter-wave Bragg reflectors. Then higher image contrast is one of advantages of EUVL, which means that masks will not require the expensive optical proximity correction (OPC) and phase shifting. Although the cost of ownership (CoO) of EUVL is lower than other methods, there are still many problems to be solved such as the source efficiency, the mirror reflectance, the incident angle, and the thickness of the multilayer.

1.2 Extreme Ultra-Violet Lithography

At normal incidence, no material provides more than about 1% reflectance in the EUV spectral region at wavelengths below 30 nm, because the index of refraction of all materials in this region is approaching unity. The original idea to use soft x-rays in the 4 nm to 40 nm wavelength range is during the 1980s [7] - [10]. In 1972, E. Spiller of IBM showed that multilayer structures composed of thin layers of materials that have widely different EUV absorption values can lead to constructive interference and therefore enhanced reflectance. In 1985, T. Barbee , S. Mrowka, and M. Hettrick changed the multilayer structure by molybdenum-silicon (Mo/Si) instead of tungsten-carbon (W/C) around 20-nm wavelength. Replacing new material coated on the wafer got a better reflectance [11]. In 1988, A. Hawryluk and L. Seppala of Lawrence Livermore National Laboratory (LLNL) invented two-mirror system. In 1989, A. Hawryluk, N. Ceglio, and D. Gaines changed the light source to 13-nm wavelength; besides, they changed the mask and the wafer from the concave spherical shape to the flat shape. In 1990, the group at AT&T tried to apply the laser technology to lithography. The second stage of EUVL development is focusing on the lager image fileds and smaller wavefront errors. The team of AT&T published the light source from the soft x-ray projection to the extreme ultraviolet. Today, ASML published the alpha demo tool and lots of companies utilized this machine to fabricate on 45-nm test chip [12].

There are several sources for EUVL, such as synchrotron, discharge-produced plasma (DPP), and laser-produced plasmas (LPP). Synchrotron source does not need frequently replace components, but its high cost and large space requirement are big problems. And another source is LPP produced by very-high-intensity pulsed-laser light and focus onto a material accompanies high temperature to create plasmas then high-energy photons are emitted. LPP use different injection laser target such as xenon, lithium, and tin [13], and usually use noble gas because it is chemically inert [14], [15]. In addition, using noble gas as the EUV radiation materials can increase the conversion efficiency. Today, tin is a dominant candidate because its high efficiency to EUV light and good reflectance in the Mo/Si multilayer. To decrease the cost of ownership for NGL, DPP was developed [16]. In an EUV lithography system, all the lenses are reflective and defect free. The surface roughness makes a great impact on the image contrast and throughput. Fortunately, the EUV imaging system consists of fewer lenses than another system. Because of coating

with repeated high-Z (Z is the atomic number) and low-Z materials can achieve a high reflectance. A pair of multilayer (i.e., Mo/Si) thickness is half the wavelength of the EUV source. If the reflectance is lower than 70%, the light intensity will be strongly reduced. In addition, we should reduce the thermal impact on the glass substrate to avoid the deformation. Lenses should not be compressed to avoid getting defects. The EUV source such as plasma with a high EUV intensity will destroy the optics. Fortunately, the laser source is distant from optics that leave the heat to protect from deformation amd extend the life time of optics. On the other hand, because of the EUV source plasma will produce erosion of multilayer, it will get much more erosion. In EUV lithography systems, there are an even number of mirrors. If it is not necessary, there is no need to add optics, because adding mirrors will decrease the transmission rate of light.

EUVL mask is a blank mask to be pattern. The fundamental properties of the blank mask are flat, defect-free, and thermal independently. It is important to consider the thermal problem because the mask absorbs EUV energy which results in the thermal expansion. The tolerance of critical defect dimension is according to 80% half-pitch technology node. Now the defect in the multilayer can be removed by focused ion beam (FIB) [17]. For the mask applications, above the Mo/Si multilayer are the absorber layer and the anti-reflective coating layer to form the low-reflectance region. Ta-based materials are good candidate as absorber layer such as TaBN, TaN and TaSi in EUVL [18], [19]. SiON, Si_3N_4 and Al_2O_3 are used as the anti-reflective coating layer [20], [21].

When the critical dimension (CD) shrink, the line edge roughness (LER) does not decrease with expected. The CD resolution and line LER are big challenges for the NGL [22], [23]. Chemically amplified resist (CAR) is used for 193 nm and 248 nm optical lithography. However, CAR absorbs EUV light which cause the LER and the pattern collapsed. Thus, poly methyl methacrylate (PMMA) is a better option for an EVL system. In addition, the pattern collapse depends on the aspect ratio, so we expect that the aspect ratio will be lager than 3 in usual, but it only achieve 2 or less in practice. Besides, there are still many challenges such as sensitivity, resolution, out-gassing and so on. Among these challenges, out-gassing not only pollutes the optics but also shrinks the lifetime of optics. Even a higher sensitivity resist would generate more byproducts as well. Recently, resist must be needed to continue to develope.

1.3 Optics of EUVL Systems

Compared to optical systems that operate at visible or near-visible wavelengths, EUVL error budgets translate into very tight figure specifications for the mirror substrates and coatings that comprise the EUVL system. The mirror surface roughness in the mid and high spatial frequency ranges is also a crucial property because it affects the imaging contrast and throughput of the lithography system. As a result, the pattern and coatings in a production-scale EUVL system must be controlled to the order of subatomic dimensions. During the past few decades, the requirements imposed on the system wavefront error, on the mirror figure, and on the reflective properties and thickness control of EUV multilayer thin films have led to enormous advancements in optical manufacturing and multilayer coating technology. Scientific areas such as solar physics, astronomy, x-ray microscopy, and plasma diagnostics that need similar instrumentation technology have greatly benefited by the improvements in EUV/x-ray optics. The EUV wavelength of illumination determinates the use of reflective optical elements as opposed to the refractive lenses used in conventional lithographic systems. Thus, EUVL tools are based on all-reflective concepts: multilayer (ML) coated optics for the illumination and projection systems, and a ML-coated reflective mask. To achieve the production-quality lithographic imaging, EUVL systems must be very well-corrected for aberrations. In EUVL, the reflective multilayers are used for applications as masks and as well as mirrors in exposure systems. Examples of high reflectance EUV mirrors for near-normal incidence operation are Mo/Be and Mo/Si multilayer that exhibit high reflectance in the 11.2-12.0 nm and 12.8-14.0 nm spectral regions, respectively [24] - [26]. The motivation behind this work is the need for optical throughput enhancement which is based on the reflectance improvement of multilayer structures in an EUV projection lithographic system. Furthermore, the ML coatings with normal-incidence experimental reflectance of 70% have been demonstrated in the 11 nm to 14 nm wavelength range.

In this study, we have designed a highly reflective multilayer with interface-engineered structure, and we also have investigated their characteristics. Here, we organize an outline of the thesis as follows. In Chapters 2, the numercial method with the transfer matrix to perform the analysis of the multilayer structures will be discussed the reflectance for the multilayer structures could be calculated from the charateristic matrix. In Chapters 3, the basic considerations of the multilayer structures for EUV lithography will be re-

viewed. In Chapter 4, kinds of multilayer structures for EUV lithography system will be discussed, and the simulation results will be given. It can be seen that the thin-film optimization techniques are essential for achieving reflectance improvements for the EUV multilayer structures. The optimization procedures employed in this thesis are an integral part of the Matlab software. The notation we have adopted to represent a period in a multicomponent stack is based on the commonly-used two-component stack at 13.5-nm wavelength, e.g. Mo/Si, where Mo is the low and Si is the high refractive index material. In Chapter 5, conclusion will be given and future work will be suggested.

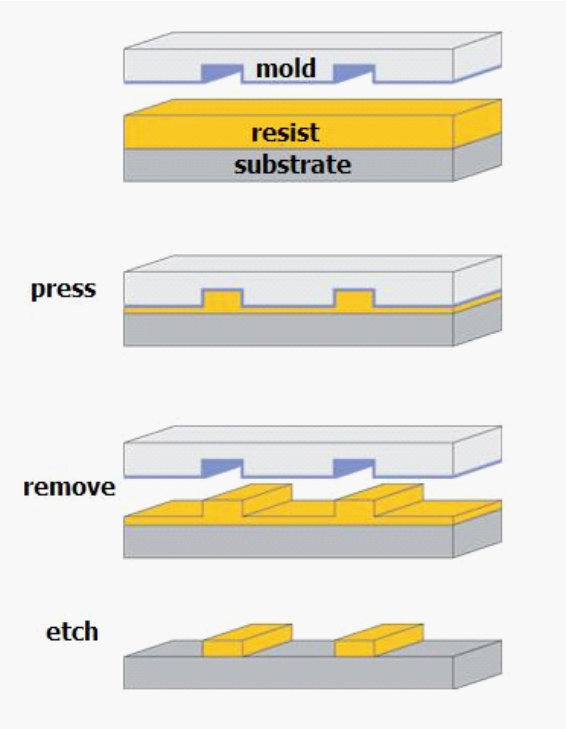

Figure 1-1: Illustration of the imprint lithography process.

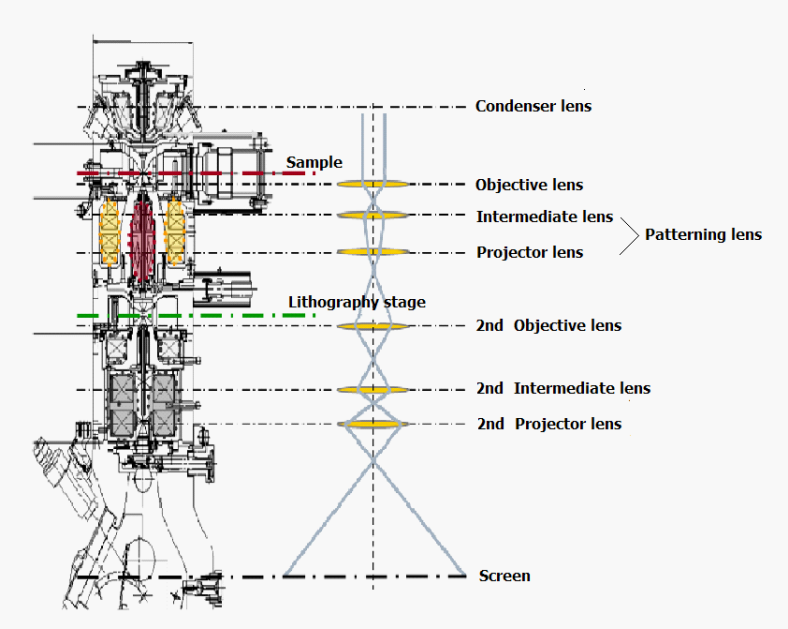

Figure 1-2: Schematic of the imprint lithography system.

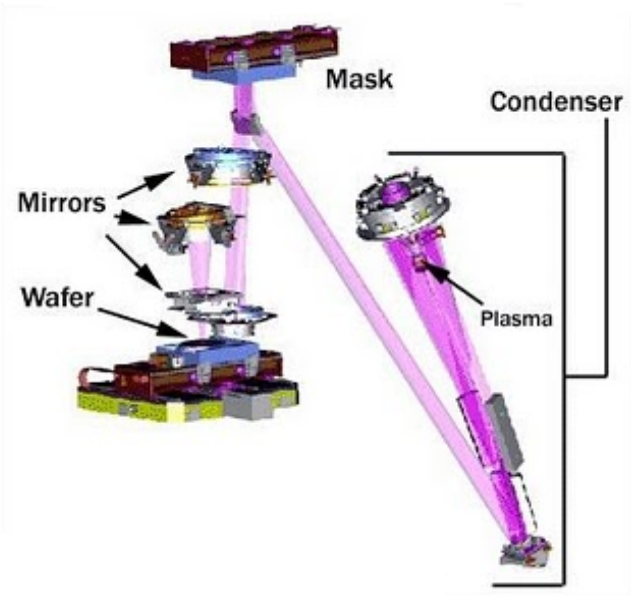

Figure 1-3: Schematic of the extreme ultra-violet (EUV) lithography system.

Chapter 2

Analytic Theories and Method

2.1 Introduction

In this chapter, we will review the method of analyzing wave propagation in an optical thin film. The transfer matrix method [28] is used to perform the analysis of multilayer structures. In order to analyze electromagnetic field in optical thin films, the polarized electromagnetic plane waves is applied. Finally, the transmittance and reflectance for the multilayer can be calculated from the charateristic matrix and observed the wave propagation behavior.

2.2 Transfer Matrix Method

The mathematical physical principles to rule the electromagnetic problems are the Maxwell's equations. For uniform dielectric and non-uniform dielectric, the Maxwell's equations (governing the electromagnetic fields) can be expressed in the following form:

$$\nabla \times E = -\frac{\partial B}{\partial t}, \tag{2.1}$$

$$\nabla \times H = J + \frac{\partial D}{\partial t}, \tag{2.2}$$

$$\nabla \cdot D = \rho, \tag{2.3}$$

$$\nabla \cdot B = 0, \tag{2.4}$$

$$J = \sigma E \ ; \ D = \epsilon E \ ; \ B = \mu H, \tag{2.5}$$

where ρ is the charge density, σ is the electrical conductivity, ϵ is the permittivity, and μ is the magnetic permeability. By solving the above equation, we can get the plane wave equation as follow:

$$\bigtriangledown \cdot \ D = \bigtriangledown \cdot \ \ (\epsilon E) = \ \epsilon \bigtriangledown \cdot E + E \cdot \bigtriangledown \epsilon = 0,$$

$$\therefore \bigtriangledown \cdot \ E \ = -E \cdot \ \frac{\nabla \epsilon}{\epsilon} = -E \cdot \nabla \left(\ln \epsilon \right),$$

and from equation $\bigtriangledown \times \bigtriangledown \times \ E = \bigtriangledown (\bigtriangledown \cdot \ E) - \bigtriangledown^2 E$, we can get

$$\bigtriangledown \times \left(-\frac{\partial}{\partial t} \mu H \right) = \bigtriangledown \left[-E \cdot \nabla \left(\ln \epsilon \right) \right] - \nabla^2 E,$$

$$\therefore -\frac{\partial}{\partial t} \left[\mu \nabla \times H + (\nabla \mu) \times H \right] = \nabla \left[-E \cdot \nabla \left(\ln \epsilon \right) \right] - \nabla^2 E,$$

$$\therefore -\left[\mu \sigma \frac{\partial E}{\partial t} + \mu \epsilon \frac{\partial^2 E}{\partial t^2} + (\nabla \mu) \times \frac{\partial H}{\partial t} \right] = \nabla \left[-E \cdot \nabla \left(\ln \epsilon \right) \right] - \nabla^2 E,$$

$$\therefore \nabla^2 E + \nabla \left[E \cdot \nabla \left(\ln \epsilon \right) \right] = \mu \sigma \frac{\partial E}{\partial t} + \mu \epsilon \frac{\partial^2 E}{\partial t^2} - \frac{\nabla \mu}{\mu} \times \left(\bigtriangledown \times E \right),$$

and assume the solution of this equation is $E = E\left(x, y, z \right) e^{i \omega t}$, then the above equation could be derived as

$$\begin{aligned} \nabla^2 E + \nabla \left[E \cdot \nabla \left(\ln \epsilon \right) \right] \ &= \ \left(i \mu \sigma \omega - \mu \epsilon \omega^2 \right) E - \nabla \left(\ln \mu \right) \times \left(\bigtriangledown \times E \right) \\ &= \ -\mu \epsilon_c \omega^2 E - \nabla \left(\ln \mu \right) \times \left(\nabla \times E \right), \end{aligned}$$

where

$$\epsilon_c = \epsilon - i \frac{\sigma}{\omega}. \tag{2.6}$$

We can get the equation of the electric field as

$$\nabla^2 E + \omega^2 \mu \epsilon_c E + \nabla \left[E \cdot \nabla \left(\ln \epsilon \right) \right] + \nabla \left(\ln \mu \right) \times \left(\nabla \times E \right) = 0, \tag{2.7}$$

and the equation of the magnetic field as

$$\nabla^2 H + \omega^2 \mu \epsilon_c H + \nabla \left[H \cdot \nabla \left(\ln \mu \right) \right] + \nabla \left(\ln \epsilon_c \right) \times \left(\nabla \times H \right) = 0, \tag{2.8}$$

and Eqs. (2.7) and (2.8) can be simplified as,

$$\nabla^2 E + \omega^2 \mu \epsilon_c E + \nabla \left[Ez \cdot \frac{\partial \ln \epsilon}{\partial z} \right] = 0, \tag{2.9}$$

$$\nabla^2 H + \omega^2 \mu \epsilon_c H + \nabla \left(\ln \epsilon_c \right) \times \left(\nabla \times H \right) = 0. \tag{2.10}$$

Figure 2-1 shows a coordinate system,which indicates the light is alone the z-direction. Relative to this geometry, we distinguished the transverse electric (TE) mode that the electric field is perpendicular to the direction of propagation and transverse magnetic (TM) mode that the magnetic field is perpendicular to the direction of propagation. In the following, we derive the wave equation governing the two mode types.

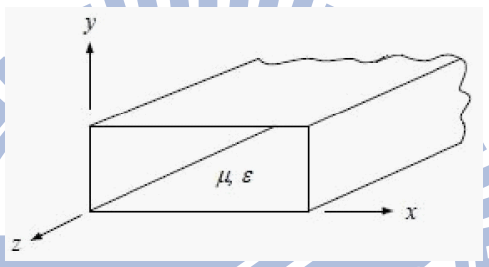

Figure 2-1: Sketch of the coordinate system, and the wave axis is chosen to coincide with the z-axis.

2.2.1 TE Mode and TM Mode

For the TE mode (also called s-polarization), we have $E_x = E_z = H_y = 0$. Then from Eqs. (2.9) and (2.10), we obtain the relations:

$$\left(\frac{\partial^2}{\partial x^2} + \frac{\partial^2}{\partial z^2} \right) E_y + \omega^2 \mu \epsilon_c E_y = 0, \tag{2.11}$$

$$\left(\frac{\partial^2}{\partial x^2} + \frac{\partial^2}{\partial z^2} \right) H_x + \omega^2 \mu \epsilon_c H_x + \frac{\partial}{\partial z} \ln \epsilon \cdot \left(\frac{\partial}{\partial x} H_z - \frac{\partial}{\partial z} H_x \right) = 0, \tag{2.12}$$

$$\left(\frac{\partial^2}{\partial x^2} + \frac{\partial^2}{\partial z^2} \right) H_z + \omega^2 \mu \epsilon_c H_z = 0. \tag{2.13}$$

For the TM mode (also called p-polarization), we have $H_x = H_z = E_y = 0$. Similarly to Eqs. (2.9) and (2.10), we obtain the relations:

$$\left(\frac{\partial^2}{\partial x^2} + \frac{\partial^2}{\partial z^2}\right) H_y + \omega^2 \mu \epsilon_c H_y - \frac{\partial}{\partial z} \ln \epsilon c \cdot \frac{\partial H_y}{\partial z} = 0, \tag{2.14}$$

$$\left(\frac{\partial^2}{\partial x^2} + \frac{\partial^2}{\partial z^2}\right) E_x + \omega^2 \mu \epsilon_c E_x + \frac{\partial}{\partial x} E_z \frac{\partial}{\partial z} \ln \epsilon = 0, \tag{2.15}$$

$$\left(\frac{\partial^2}{\partial x^2} + \frac{\partial^2}{\partial z^2}\right) E_z + \omega^2 \mu \epsilon_c E_z + \frac{\partial}{\partial z} E_z \frac{\partial}{\partial z} \ln \epsilon + E_z \frac{\partial^2}{\partial z^2} \ln \epsilon = 0, \tag{2.16}$$

2.2.2 Reflection and Transmission Coefficients

For a stack of thin, plane, parallel films of materials covering the surface of a substrate as shown in Figure 2-2, the refractive indexs are N_j and the layer thicknesses are d_j, where $j = 1$ to m. For discussing easily, we assume that there is only a single thin film layer of index N between the substrate (interface b) and incident medium (interface a), the whole dielectric is uniform and isotropy and the surface is parallel and infinite extensibility as shown in Figure 2-3 [27]. To the form of the plane wave can be described as

$$e^{i\left[\omega t - \frac{2\pi}{\lambda} N z\right]} \propto e^{-i\frac{2\pi}{\lambda} N z} = e^{-i\delta},$$

where the phase difference is $\delta = \frac{2\pi}{\lambda} N d$.

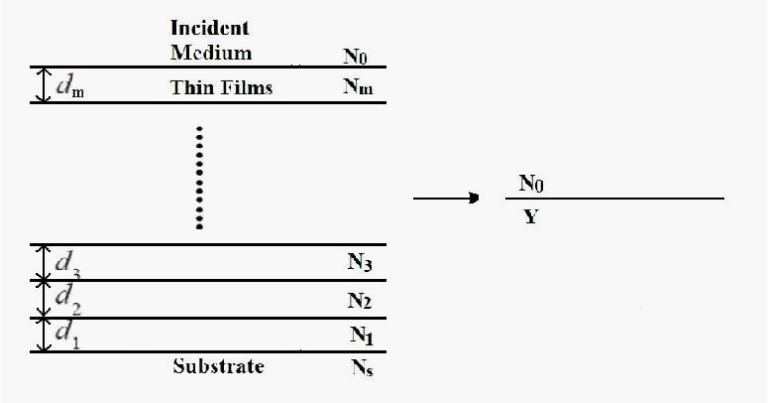

Figure 2-2: Sketch of the m-layer multilayer structure.

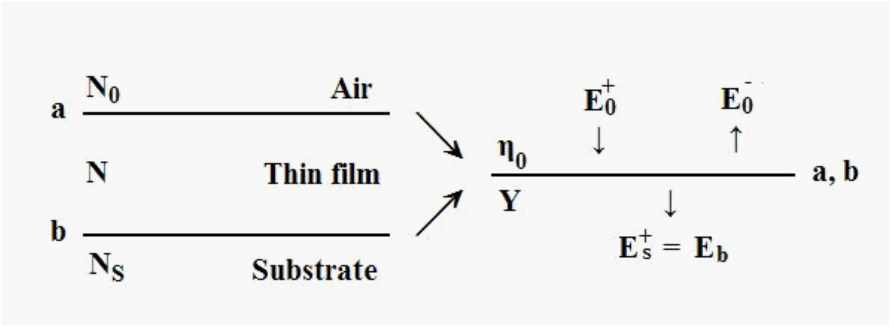

Figure 2-3: Sketch of the equivalent admittance of interfaces a and b.

For the normal incidence, the electromagnetic fields E and H are continuous at the interfaces, and we can get the relations as follows:

interface b :

$$E_b = E_{sb}^+ = E_{1b}^+ + E_{1b}^-, \tag{2.17}$$

$$H_b = H_{sb}^+ = H_{1b}^+ + H_{1b}^-,$$

$$\text{or } \eta_s E_b = \eta_s E_{sb}^+ = \eta E_{1b}^+ - \eta E_{1b}^-, \tag{2.18}$$

interface a :

$$E_a = E_{0a}^+ + E_{0a}^- = E_{1a}^+ + E_{1a}^-, \tag{2.19}$$

$$H_a = H_{0a}^+ + H_{0a}^- = H_{1a}^+ + H_{1a}^- = \eta_0 E_{0a}^+ - \eta_0 E_{0a}^- = \eta E_{1a}^+ - \eta E_{1a}^-, \tag{2.20}$$

where η_0, η, and η_s are the optical admittance of incident medium, thin films and substrate, respectively. There is a phase difference δ between surfaces a and b when the electric fields across the thin film. So we have the relation

$$E_{1a}^+ = E_{1b}^+ e^{i\delta}, \tag{2.21}$$

$$E_{1a}^- = E_{1b}^- e^{-i\delta}. \tag{2.22}$$

From Eqs. (2.17) and (2.18), we can get

$$E_{1b}^+ = \frac{\eta E_b + H_b}{2\eta} \text{ and } E_{1b}^- = \frac{\eta E_b - H_b}{2\eta},$$

then

$$\begin{aligned} E_a &= E_{1a}^{+} + E_{1a}^{-} = E_{1b}^{+} e^{i\delta} + E_{1b}^{-} e^{-i\delta} \\ &= \frac{\eta E_b + H_b}{2\eta} e^{i\delta} + \frac{\eta E_b - H_b}{2\eta} e^{-i\delta} \\ &= E_b \cos\delta + H_b \left(\frac{i \sin\delta}{\eta} \right), \end{aligned} \tag{2.23}$$

$$\begin{aligned} H_a &= H_{1a}^{+} + H_{1a}^{-} = \eta E_{1b}^{+} e^{i\delta} - \eta E_{1b}^{-} e^{-i\delta} \\ &= \frac{\eta E_b + H_b}{2} e^{i\delta} - \frac{\eta E_b - H_b}{2} e^{-i\delta} \\ &= E_b (i\eta \sin\delta) + H_b \cos\delta. \end{aligned} \tag{2.24}$$

Eqs. (2.23) and (2.24) can be written as vector form M as

$$\begin{bmatrix} E_a \\ H_a \end{bmatrix} = \begin{bmatrix} \cos\delta & \frac{i}{\eta}\sin\delta \\ i\eta \sin\delta & \cos\delta \end{bmatrix} \begin{bmatrix} E_b \\ H_b \end{bmatrix}, \tag{2.25}$$

and the characteristic matrix of the single film is

$$M = \begin{bmatrix} \cos\delta & \frac{i}{\eta}\sin\delta \\ i\eta \sin\delta & \cos\delta \end{bmatrix}. \tag{2.26}$$

Then from Eqs. (2.19) and (2.20), we have the relations

$$E_{0a}^{+} = \frac{\eta E_a + H_a}{2\eta_0} \text{ and } E_{0a}^{-} = \frac{\eta_0 E_a - H_a}{2\eta_0}.$$

Once the charateristic matrix of a multilayer stack is known, one can easily determine the reflection and transmission coefficients for light incident on the stack. Hence, the reflection and transmission coefficients are derived as follows, respectively.

$$\rho = \frac{E_{0a}^{-}}{E_{0a}^{+}} = \frac{\eta_0 E_a - H_a}{\eta_0 E_a + H_a} = \frac{\eta_0 - Y}{\eta_0 + Y}, \tag{2.27}$$

$$\tau = \frac{E_b}{E_{0a}^{+}} = \frac{2\eta_0 E_b}{\eta_0 E_a + H_a} = \frac{2\eta_0 \frac{E_b}{E_a}}{\eta_0 + Y}. \tag{2.28}$$

Both sides of Eq. (2.25) are divided by E_b, where $Y_b = \frac{H_b}{E_b}$ which is equal to the admittance of the substrate (Y_s); then rewriting Eq. (2.25), we can obtain

$$\begin{bmatrix} B \\ C \end{bmatrix} = \begin{bmatrix} \cos\delta & \frac{i}{\eta}\sin\delta \\ i\eta\sin\delta & \cos\delta \end{bmatrix} \begin{bmatrix} 1 \\ Y_s \end{bmatrix}, \tag{2.29}$$

where the equivalent admittance Y is $\frac{C}{B}$. Then we have

$$\rho = \frac{\eta_0 B - C}{\eta_0 B + C}, \text{ and } \tau = \frac{2\eta_0}{\eta_0 B + C}.$$

Therefore, we have the reflectance and the transmittance from the above equations as:

$$R = |\rho|^2 = \left(\frac{\eta_0 B - C}{\eta_0 B + C}\right)\left(\frac{\eta_0 B - C}{\eta_0 B + C}\right)^*, \tag{2.30}$$

$$T = \frac{\mathrm{Re}(Y_s)}{Y_0}|\tau|^2 = \frac{4\eta_0\,\mathrm{Re}(Y_s)}{(\eta_0 B + C)(\eta_0 B + C)^*}. \tag{2.31}$$

Matrix calculations determine the transmittance and reflectance profile for multilayer structures on a substrate. Consider a loss free multilayer design, normally incident radiations, and assume that films are optically homogenous. The electric field vector (E_m) and the magnetic field vector (H_m) at the incident boundary of a film at the boundary by the product of the following matrices per layer. The matrix is calculated at each boundary throughout the multilayer as the magnitude of electric and magnetic field vectors alter with the properties of the layer [28]. Application of the appropriate boundary conditions between each layer requires that the tangential components of E and H vectors are continuous across each boundary to the equations of wave propagation. The fields at other interfaces $m-1$ are similar to Eqs. (2.23) and (2.24) at the same instant of time and a position with identical x and y coordinates.

And we can obtain the matrix form between the $(m-1)$-th layer and $m-$th layer as

$$\begin{bmatrix} E_{m-1} \\ H_{m-1} \end{bmatrix} = \begin{bmatrix} \cos\delta_m & \frac{i}{\eta_m}\sin\delta_m \\ i\eta_m\sin\delta_m & \cos\delta_m \end{bmatrix} \begin{bmatrix} E_m \\ H_m \end{bmatrix}.$$

Solving the above given expressions, the matrix expression for single layer is:

$$M = \begin{bmatrix} E & iF \\ iG & H \end{bmatrix},$$

where: $\cos\delta_m = E = H$, $i\sin\delta_m/\eta_m = F$, $i\eta_m\sin\delta_m = G$.

For a multilayer containing m layers, we have

$$\begin{bmatrix} E_0 \\ H_0 \end{bmatrix} = M_1 M_2 M_3 \cdots\cdots M_m \begin{bmatrix} E_m \\ H_m \end{bmatrix} = M \begin{bmatrix} E_m \\ H_m \end{bmatrix},$$

where

$$M = \prod_{j=1}^{m} M_j = \prod_{j=1}^{m} \begin{bmatrix} \cos\delta_j & \frac{i}{\eta_j}\sin\delta_j \\ i\eta_j \sin\delta_j & \cos\delta_j \end{bmatrix}. \tag{2.32}$$

From Eq. (2.29), $\begin{bmatrix} B \\ C \end{bmatrix}$ is known as the charateristic matrix of the assembly. Then the transmittance and reflectance for the multilayer can be calculated from this product matrix by:

$$R = \left(\frac{\eta_0 B - C}{\eta_0 B + C}\right)\left(\frac{\eta_0 B - C}{\eta_0 B + C}\right)^*, \tag{2.33}$$

$$T = \frac{2\eta_0 \,\mathrm{Re}(Y_s)\,(BC^* + B^*C)}{(\eta_0 B + C)\,(\eta_0 B + C)^*} \cdot \frac{2}{(BC^* + B^*C)} = \frac{4\eta_0 \,\mathrm{Re}(Y_s)}{(\eta_0 B + C)\,(\eta_0 B + C)^*}. \tag{2.34}$$

Sufficient information is included in Eqs. (2.33) and (2.34) to allow the reflectance and transmittance of a thin-film assembly to be calculated. The reflectance, transmittance, and absorptance are then related by $R + T + A = 1$. The solution of this matrix theory is for multilayer coatings. However, insight into the properties of thin-film assembles cannot easily be gained simply by feeding the calculations into a computer program, and insight is necessary if multilayers are to be designed and if their limitations in use are to be fully understood. An approximate method has also been found useful. Based on the matrix theory, in this thesis we have developed a program by MATLAB 7.1 to design and simulate the performance of multilayer coatings.

Chapter 3

Multilayer Consideration for EUVL

3.1 Introduction

EUV lithography (EUVL) employs illumination wavelengths around 13.5 nm, and in many aspects it is considered an extension of optical lithography, which is used for the high-volume manufacturing (HVM) of today's microprocessors. The EUV wavelength of illumination dictates the use of reflective optical elements (mirrors) as opposed to the refractive lenses used in conventional lithographic systems. Thus, EUVL tools are based on all-reflective concepts: multilayer (ML) coated optics for the illumination and projection systems, and a ML-coated reflective mask.

3.2 Basic Principle of Multilayers

The basic principle behind the optical design in multilayer mirror is simple. A multilayer is an artificial structure with a large number of interfaces. A single interface reflects a small fraction of an incident beam; however, the reflectance increases dramatically if the reflected beams from all the interfaces in the multilayer add in phase. The predominant designs are composed of distributed Bragg condition resembling quarter wavelength stacks with constant film thicknesses. These reflectance values whilet adequate for optical systems with a few reflectors will dramatically diminish the output optical intensity to 6-10% directly before the first mirror in a nine-mirror EUV lithographic system. Therefore, it is evident that even an increase of 1-2% in the peak reflectance of a single mirror will yield a significant light throughput enhancement in the overall optical system. A

particular problem in the EUV region is that all useful materials absorb the radiation to a certain extent. To reduce the effect on the reflectance response of the absorption losses, the thicknesses of the two components of the stack are adjusted to deviate slightly from the optical path length of $\lambda/4$. The highest reflectance is usually achieved by choosing materials with the largest difference in refractive indices and extinction coefficients. This means that one material is more absorbing (as spacer layer) while the other material is more transparent (as absorber layer) . For the EUV range, the best material pair seems to be Mo and Si. The thickness of the high absorption layer d_{h} is set slightly lower than that of the low absorption layer d_{l}, thus the partition ratio $\Gamma = d_{\mathrm{h}}/(d_{\mathrm{h}} + d_{\mathrm{l}})$ of the multilayer is defined. Vinogradov and Zeldovich [29] have calculated Γ as a function of absorption - a value of $\Gamma = 0.4$ is commonly used. Also, it is well known for general thin-film mirror designs with absorbing films and for EUV designs, that a gradual variation of the partition ratio through the stack with $\Gamma = 0.3 - 0.4$ at the surface to $\Gamma = 0.5$ near the substrate can increase the peak reflectance. Such optimized stacks would yield significant throughput enhancements in a nine-mirror optical system.

Up to date, there are several ways to increase the reflectance for Mo/Si multilayer which is the most common reflectors in soft x-ray range:

(1) Add some extra materials into the prime stack.

(2) One material with better optical constants (i.e. less absorption/small k) is substituted for a material on the fundamental stack.

(3) Using some optimized algorithms to calculate the optimum partition ratio Γ of each pair, and its thickness of each pair in the multilayer.

(4) Using a capping layer which is inactivate to the thin film layer can avoid the surface oxidation that led to the reduction of reflectance in multilayers.

Once Spiller [24] showed that quarter-wave stacks of absorbing materials can be used effectively as optics in the EUV and soft x-ray regions. In the approximation, the highest reflectance is achieved with a material pair that has a minimum absorption and a maximum difference in the refractive indices among the constituent materials. The theory of quasi-quarter-wave MLs predicts enhanced EUV reflectance at 13.5 nm based on the use of thin films of several materials with the largest possible refractive index differences. However, such MLs have often performed better only in theory. Other factors, such as the roughness, interdiffusion, chemical reactivity, and lifetime stability of the layer interfaces,

also play the important roles in the ML film performance. The enhanced reflectance was demonstrated and studied in MLs with diffusion barrier layers, whose primary function was to suppress interdiffusion. Reflectance can also be optimized by varying the layer thickness ratio of the individual materials. If MLs must be thermal or radiation stable, the design requires the use of refractive materials such as oxides, carbides, silicides, and alloys, or the introduction of barrier layers that are deposited on interfaces to reduce the interdiffusion due to elevated temperatures. High-resolution MLs can be achieved by selecting materials with a certain ratio of optical constants, by optimization of layer thickness and of the number of bilayers, and by using higher-reflectance orders from ML structures. A wide spectral bandwidth requires a periodic ML design.

3.3 Choice of Multilayer Materials and Wavelength Considerations

Methods for transmission mode x-ray analysis of a sample by means of apparatuses comprising an x-ray radiation source that provides x-ray radiation for irradiating the sample and a detector for detecting x-ray radiation transmitted through by the sample. Figure 3-1 shows a schematic with the intensity I_0 of incident x-ray and the intensity I_t of being transmitted through by the sample.

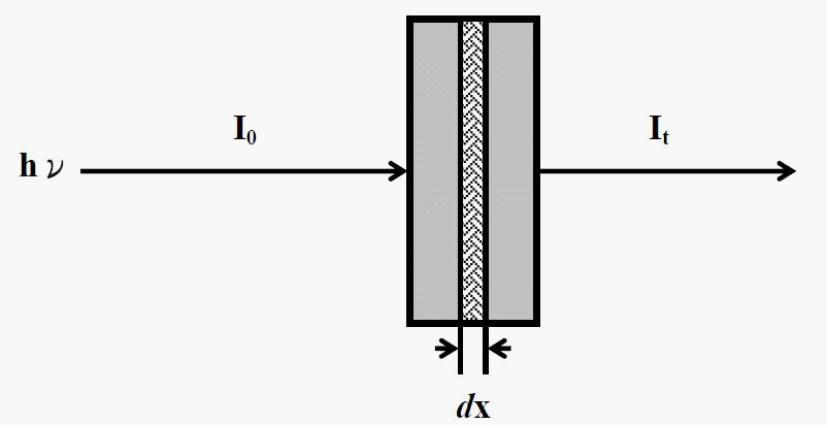

Figure 3-1: Schematic with the intensity I_0 of incident x-ray and the intensity I_t of being transmitted through by the sample.

A narrow parallel monochromatic x-ray beam of intensity I_0 passing through a sample of thickness dx will get a reduced intensity I_t according to the expression:

$$dI_t = -I_0(x) \cdot n \cdot \sigma \cdot dx, \tag{3.1}$$

where dI_t is the change in intensity, I_0 is the initial intensity, n is the number of atoms/cm^3, σ is a proportionality constant that reflects the total probability of a photon being scattered or absorbed and dx is the incremental thickness of material transversed. When this equation is integrated, it becomes:

$$I_t = I_0 \exp(-n\sigma x), \tag{3.2}$$

The number of atoms/cm^3 (n) and the proportionality constant (σ) are usually combined to yield the linear attenuation coefficient (μ). Therefore the equation becomes:

$$I_t = I_0 \exp(-\mu x). \tag{3.3}$$

where I_t is the intensity of photons transmitted across some distance x, I_0 is the initial intensity of photons, μ is the linear attenuation coefficient, and x is distance traveled.

The linear attenuation coefficient (μ) describes the fraction of a beam of x-rays or gamma rays that is absorbed or scattered per unit thickness of the absorber. This value basically accounts for the number of atoms in a cubic cm volume of material and the probability of a photon being scattered or absorbed from the nucleus or an electron of one of these atoms. Using the transmitted intensity equation above, linear attenuation coefficients can be used to make a number of calculations. These include:

(1) the intensity of the energy transmitted through a material when the incident x-ray intensity, the material and the material thickness are known.

(2) the intensity of the incident x-ray energy when the transmitted x-ray intensity, material, and material thickness are known.

(3) the thickness of the material when the incident and transmitted intensity, and the material are known.

(4) the material can be determined from the value of μ when the incident and transmitted intensity, and the material thickness are known.

Figure 3-2 is an illustration of linear attenuation coefficient (μ) versus wavelength (λ) and we can find that μ is as a function of λ for every material; however, the extinction coefficient k (the imaginary part of refractive index) is proportional to the linear attenuation coefficient μ in accordance with Eq. (3.5). The refractive index is complex, the extinction coefficient introduces a decrease of the amplitude of the waves passing through the material and phase changes between the incident and successively reflected waves.

$$N = 1 - \delta - i\beta = n - ik,$$

where $1 - \delta$ (n) is the real part of refractive index and β (k) is the imaginary part of refractive index. And more specifically definitions are

$$\delta = r_e \frac{\lambda^2}{2\pi} N_a f_2^0 \text{ and } \beta = r_e \frac{\lambda^2}{2\pi} N_a f_2^0 \equiv \frac{\lambda\mu}{4\pi}, \tag{3.4}$$

$$\mu = r_e \frac{2\lambda}{Am_u} f_1^0, \tag{3.5}$$

where r_e is classical electron radius, N_a is the Avogadro's number, m_u is the atomic mass unit, and f_1^0 and f_2^0 are the anomalous dispersion correction factors. And the detail datas above see Appendix.

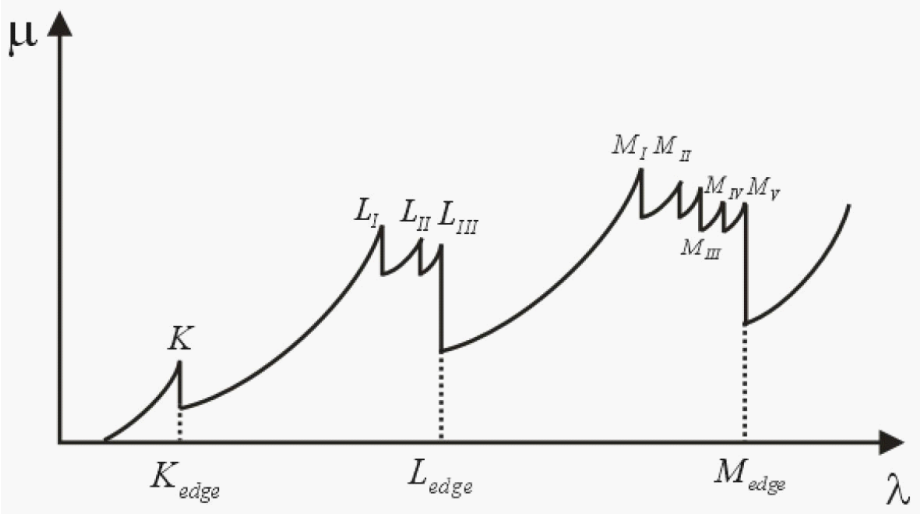

Figure 3-2: Schematic progression of the linear absorption coefficient of wavelength.

Hence, we regard the figure as a relation chart of extinction coefficient and wavelength underlying the x-ray spectrum. At certain energies where the absorption increases drastically, and gives rise to an absorption edge. Each such edge occurs when the energy of the incident photons is just sufficient to cause excitation of a core electron of the absorbing atom to a continuum state, i.e. to produce a photoelectron. Thus, the energies of the absorbed radiation at these edges correspond to the binding energies of electrons in the K, L, M, etc, shells of the absorbing elements. See Figure 3-3, the absorption edges are labelled in the order of increasing energy, K, L_I, L_{II}, L_{III}, M_I, ..., corresponding to the excitation of an electron from the 1s ($^2s_{1/2}$), 2s ($^2s_{1/2}$), 2p ($^2p_{1/2}$), 2p ($^2p_{3/2}$), 3s ($^2s_{1/2}$), ... orbitals (states), respectively. In other words, the absorption effect of materials would apparently lower and its the key to choose what kind of reflector would be in each spetrum.

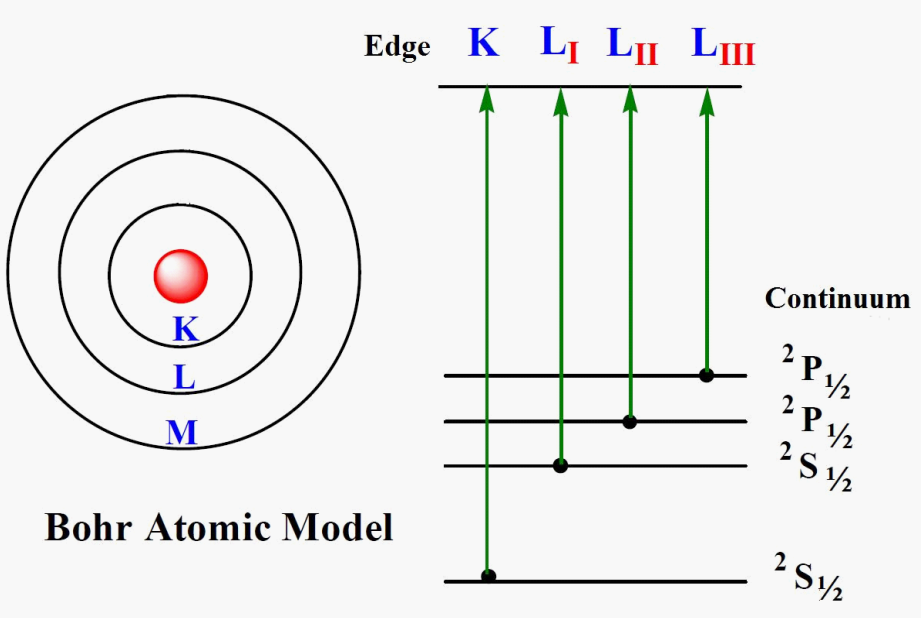

Figure 3-3: The left side is a simplified illustration of Bohr atomic model and the right side is a comparison of continuum level versus absorption edge overplotted.

We called a light element as spacer (i.e. silicon) that absorbs light only weakly, and a heavy element as absober (i.e. molybdenum) that absorbs light very strongly. However, the reason should be considered is not only the extinction coefficient but easily form an stable and/or sharp interface with other element. At present, the materials of silicon (Si), beryllium (Be), boron (B) and carbon (C) are commonly used for spacer layer. And the

combination of spacer layer is called absorber layer, as well as the extinction coefficient is much larger than spacer layer. To choose those materials have large difference of extinction coefficient but small one is to avoid the incident light would be absorbed completely, thus the reflectanec can not be improved. Figure 3-4 [30] is all different types of general x-ray reflectors with its suitable energy (wavelength). The illumination wavelength of 13.5 nm was chosen for EUV lithography based on the early development and good performance of molybdenum-silicon MLs in this wavelength region. Mo/Si still remains the most extensively investigated and best understood ML material pair to date, and 13.5 nm is in the wavelength region just longer than the $L_{2,3}$ absorption edge of Si (12.4 nm), where Mo/Si achieves its best reflective performance. In addition, the first available sources for EUVL were LPP sources, with good conversion efficiency in this wavelength region. Even though the output of the LPP source at 13.5 nm was lower than at 11 nm, the natural width of the Bragg peak of a Mo/Si ML at 13.5 nm is broader than the peak width of a Be-based ML at 11 nm. Hence, the overall integrated reflectance is comparable at both 11-nm and 13.5-nm wavelengths. The broader peak width at 13.5 nm also relaxes specifications for optic-to-optic wavelength matching. There are othe benefits associated with operating at 13.5 versus 11 nm.

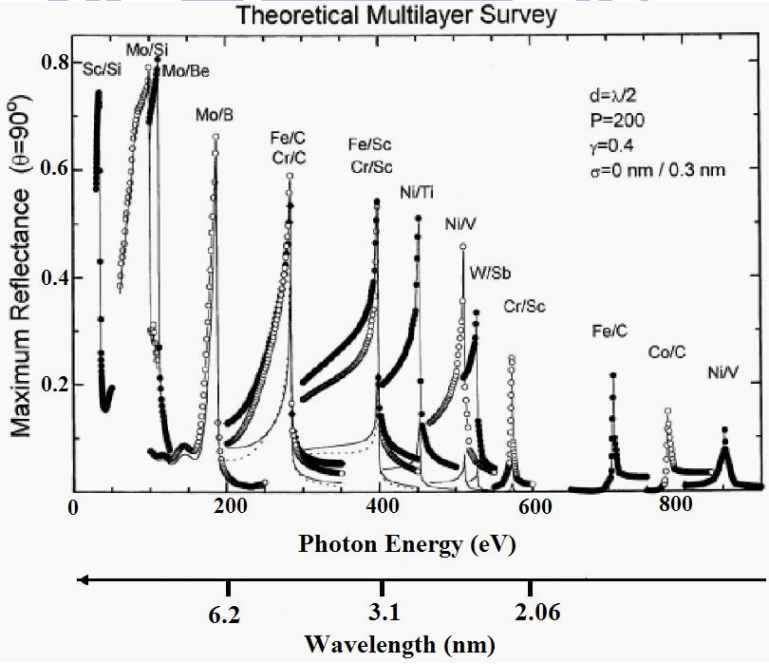

Figure 3-4: Theoretical multilayer survey: Maximum achieveable normal incidence reflectance in the soft x-ray range for the systems shown.

3.4 Multilayer Deposition Technologies

It is well known that the reflectance of ML mirrors does not depend only on the materials being used but also on the structural quality of the coatings. Coating quality depends on the deposition method (magnetron-beam sputtering, ion-beam sputtering, electron-beam evaporation, pulsed laser deposition) and the overall deposition control. The first ML structures were made by physical vapor deposition (PVD). A nice overview of PVD methods, including thermal and sputter vapor depositions, can be found in Barbee's review paper. Another way to deposit thin films and ML coatings is chemical vapor deposition (CVD), although this technique involves complex chemistry and chemical reactions, often requires a high deposition temperature, and traditionally does not been used to produce EUV MLs. The most commonly used deposition technique for EUVL mirrors is magnetron sputtering. High-quality Mo/Si MLs were already achieved in the mid-1980s. The advantages of this technique are the ability to coat large optics, great control, the stability of the sources, reproducibility from run to run, and a relatively fast sputtering rate. The first EUVL optics sets for 0.1-NA full-field systems and 0.3-NA microfield systems were fabricated using magnetron deposition. An example of a DC-magnetron sputtering system optimized for the coating of large area optics is shown in Figure 3-5 [31]. Similar mirrors for an EUVL process development tool were coated using e-beam evaporation in combination with ion-beam smoothing. High-quality EUV ML coatings are also obtained with ion-beam deposition and ion-assisted deposition. This technique is primarily used to coat EUVL mask blanks because it is a low-defect process. Because of the high energy of impacting ions, this technique also enhances smoothing by increasing the motion of the atoms on the surface. With additional ion polishing, such a technique can relax the requirement for the surface finish of EUV optics and mask substrates. Another technique is pulsed laser deposition (PLD). Other modes of film deposition—though not yet demonstrated—may be possible (e.g., atomic layer deposition (ALD), molecular beam epitaxy (MBE), and modified chemical vapor deposition (CVD) arrangements).

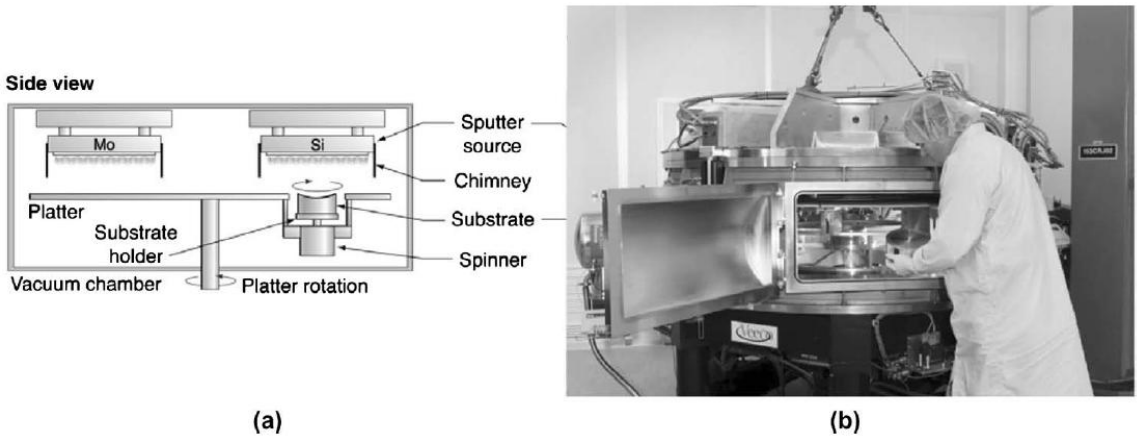

Figure 3-5: (a) Side view of the LLNL large-optics DC-magnetron sputtering system. (b) An optic introduced into the chamber through a side door.

3.5 Optical Constants

To successfully model and predict the performance of ML coatings for EUVL, precise knowledge of the optical properties of a system's constituent materials is required. The absorptive and dispersive behavior of each material can be obtained from the real and imaginary part of the wavelength-dependent refractive index, also known as optical constants. In the EUV/x-ray region, where the wavelength of radiation is comparable to the binding energies of the inner electrons in the material, measurements of the refractive index can be particularly challenging due to sensitivity to surface oxides, contamination, and roughness of the material samples under study. Although sophisticated models have been developed to determine the refractive index of materials using first-principles calculations, experimental measurements are always recommended as the best method to accurately determine the refractive index of vapor-deposited thin films. This is especially true for energy regions in the electronic absorption edges, where the optical properties can strongly depend on experimental conditions such as the method and environment of deposition. The optical constants of important EUVL materials for ML coatings such as Si [32], Mo [33], [34] and Ru [35] have been updated in recent years with more accurate experimental results. A comprehensive compilation of the optical constants for all elements in the periodic table, including recently obtained data, are maintained in the Center for X-Ray Optics (CXRO) database [36]. Other databases for the optical properties of materials in the EUV/x-ray region are maintained by the National Institute of

Standards and Technology (NIST) [37] and LLNL [38]. The values of n, k at the EUV wavelengths of particular interesting materials are tabulated in Table 3.1.

Table 3.1: Values of n and k at 13.5 nm.

	13.5 nm	
	n	k
Mo	0.9239	0.0064
Si	0.9999	0.0018
B_4C	0.9638	0.0051
C	0.9616	0.0069
Ru	0.8863	0.0171
Pt	0.8907	0.0601
SiO_2	0.9781	0.0108
Rh	0.8751	0.0312

3.6 Throughput

An EUVL scanner consists of an all-reflective optical system with ML coatings on the projection (imaging) elements, on the condenser/illuminator assembly, and on the mask. All of these elements should be tuned to reflect at or near the same wavelength to obtain a substantial output from the system. Any spectral mismatch between the mirrors would translate to throughput reduction. If a goal is set to match the reflectance peak position of all EUVL optics to within $\Delta\lambda = \pm 0.05$ nm, then in a system with six reflections, for example, this level of wavelength matching would ensure at least 97.4% of the ideal throughput. Meeting this goal requires atomic-level repeatability of the coating process from one deposition run to another. In addition to optic-to-optic wavelength matching, another throughput constraint is the tolerance on wavelength variation across the surface of any individual optic in the system. For maximum throughput, the ML should have its reflectance peak at the same wavelength for all surface points on any given mirror. If an arbitrary goal is set to stay within 99% of the reflectance peak for all points on the optic surface, then a Mo/Si ML operating at $\lambda = 13.5$ nm is allowed to have its wavelength vary to within $\Delta\lambda = \pm 0.05$ nm, which is equivalent to having the wavelength (or the thickness) vary from its prescribed value to within $\pm 0.37\%$ peak-to-valley (P-V) across the surface.

In the EUVL tools, with a vacuum of about 10^{-5} Pa, the surfaces of such multilayer-coated mirrors are exposed to EUV radiation in the presence of residual contaminants

(water vapor and hydrocarbons primarily), which lead to optics contamination (oxidation and carbon deposition). At EUV wavelengths, even a small increase in oxide or carbon layer of only few nanometers could cause a measurable reflectance decrease. Nonetheless, reflectance has to be stable within 1% in high volume manufacturing (HVM) lithography because the optical throughput is proportional to:

$$\int \prod_{j=1}^{m} R^j(\lambda) d\lambda, \tag{3.6}$$

where R is the reflectance of the $m-$th multilayer mirror and j is the number of reflective mirrors in the EUVL tool (Figure 1-3).

These HVM tools might contain 7 or more reflective mirrors, and any small change in reflectance will lead to a noticeable change in the throughput. Hence, optics lifetime is one of the critical issues for the success of this technology and different strategies to obstruct oxidation and contamination have been studied [39] - [41]. To extend the lifetimes of the projection optics is by coating the multilayers with thin 2~3-nm capping layer [42] - [44] films (Figure 3-6) that reduce the buildup of contamination. In this thesis, we evaluate the solid phase elements in the periodic table and their material combinations as possible capping layer candidates for EUVL applications.

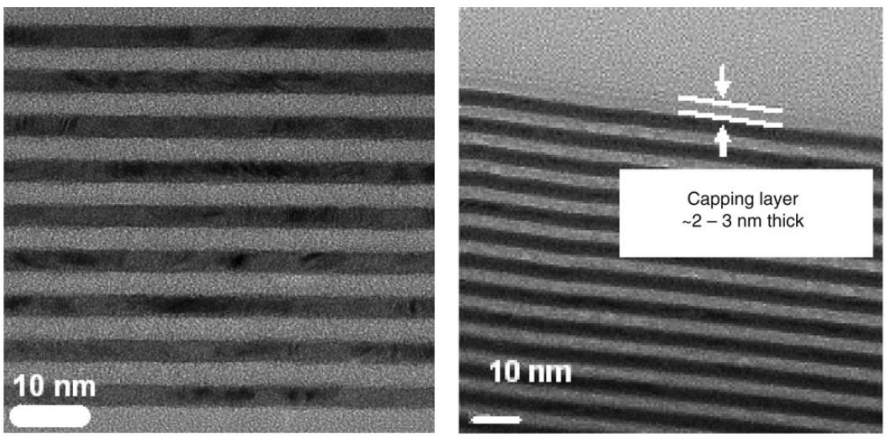

Figure 3-6: TEM cross-section of a Mo/Si multilayer is showing crystalline Mo and amorphous Si. The right image shows the top part of the multilayer, including the capping layer.

Chapter 4

Multilayer Design for High Reflectance in EUV Lithography

4.1 Introduction

Over the past few decades, several lithography techniques have been investigated as substitutes for conventional optical lithography. Among these next generation lithography techniques (NGL), extreme ultraviolet lithography (EUVL) has been considered as one of the most competitive technology owing to its high throughput, similarities with conventional optical lithography, and robust mask structure. In EUVL, the reflective multilayer structures are used for applications as masks as well as mirrors in exposure systems. Reflectance of these multilayers, which is a critical factor for throughput of the EUVL, depends on the structure factors as well as on the material properties.

4.2 Mo/Si Multilayer Structure for EUV Lithography

4.2.1 Design Consideration for a Mo/Si Multilayer Structure

At present, there is a considerable interest in mirrors with high reflectance at near-normal incidence tuned for the extreme-ultraviolet (EUV) spectral region, most particularly in the $11 - 14$ nm range. This interest is driven by the potential of EUV projection lithography as the basis for the next generation of high-throughput semiconductor lithographic

tools for fabricating structures below 70 nm. The design of thin-film multilayer reflectors for the EUV spectral region has been extensively studied by Spiller [24]. Of particular importance for EUV projection lithographic applications are the two-component Mo/Be and Mo/Si multilayer systems that exhibit particularly high theoretical reflectance in the $11.3 - 11.6$ nm and $13.0 - 13.6$ nm spectral regions, respectively. The reflector designs are composed of distributed Bragg reflectors resembling quarter-wavelength stacks with constant film thicknesses throughout. The typical designs that have been fabricated are 80 periods of Mo/Be and 40–50 periods of Mo/Si. These designs yield maximum theoretical reflectance of $R \sim 78\%$ for the Mo/Be stack and $R \sim 74\%$ for the Mo/Si stack. These reflectance values which are among the best for multilayer reflectors in the EUV region, although adequate for optical systems with a few reflectors, will dramatically diminish the output optical intensity to 6–10% of that directly before the first mirror. The significance of nine near-normal incidence mirrors is that the number envisaged for an EUV lithography system: two in the illumination optics, six in the imaging optics plus the reflecting reticle. It is evident that even a small increase of 1–2% in the peak reflectance of a single mirror will yield a significant light throughput enhancement in the optical system.

For Bragg reflectors with non-absorbing films the optimum optical path difference within each film would be a quarter-wavelength. However, a particular problem in the EUV region is that all useful materials absorb the radiation to a certain degree. To reduce the effect on the reflectance response of the absorption losses, the thicknesses of the two components of the stack are adjusted slightly from the optical path length of a quarter wavelength. The thickness of the high-absorption layer d_{h} (commonly called the absorber layer) is set slightly lower than that of the low absorption layer d_{l} (commonly called the spacer layer); thus the partition ratio $\Gamma = d_{\mathrm{h}}/(d_{\mathrm{h}} + d_{\mathrm{l}})$ of the multilayer is defined. A typical multilayer consists of $40 - 60$ repeats of this period and usually ends with a Si layer, which partially oxidizes when exposed to air. Mo and Si layers usually act as the absorber layer and the spacer layer, respectively. And the thickness of Mo is designed thinner than that of Si due to the stronger absorption in EUV range. It reveals that the reflectance of the EUV multilayer mirror depends on the accurate thicknesses of the stacked layers. The thicknesses of the stacked layers through optimized design can provide the highest reflectance for a given wavelength. The pairs of materials, the periodic

thickness of the multilayer, the thickness ratio, and even the interface roughness are the factors that should be taken into consideration for an optimized design. Figure 4-1 is a illustraion of reflective multilayers used for applications as masks and as well as mirrors in exposure systems and Figure 4-2 shows a schematic diagram of the Mo/Si EUV reflective multilayer structure. The thickness ratio has a most significant meaning in making a multilayer mirror due to its position of the peak wavelength is mainly determined. In a real lithographic system, which consists of several mirrors, the matching of the thickness ratio in each mirror in accordance with the position of the peak wavelength and the intensity distribution of the reflected light is critical for reflectance and throughput.

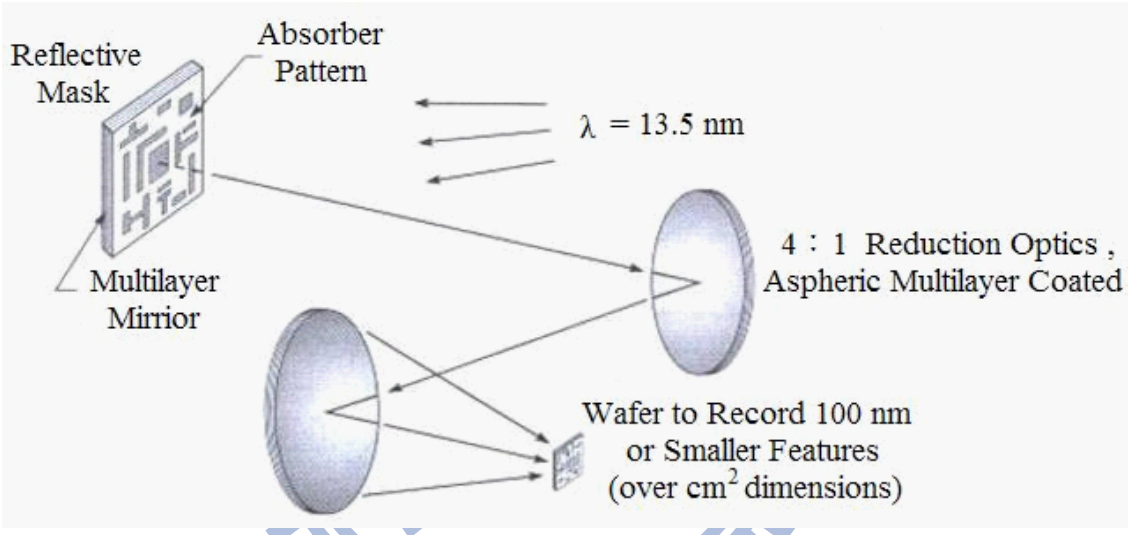

Figure 4-1: The simple schematic illustration of an EUVL projection system.

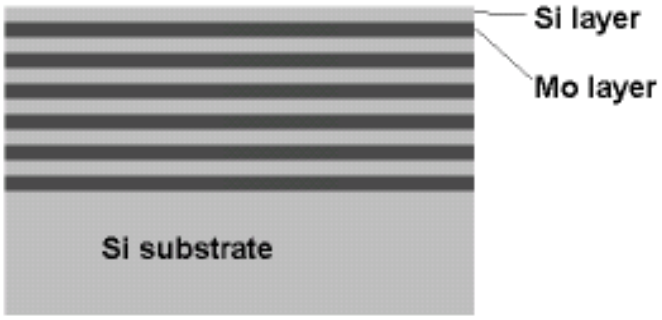

Figure 4-2: The schematic diagram of the Mo/Si multilayer.

4.2.2 Reflectance Optimization for a Mo/Si Multilayer Structure

The simulation results in this thesis were all performed by using the language of technical computing design program MATLAB 7.1 (The MathWorks, Inc.), which is based on the characteristic matrix methodology [27] as discussed in Chapter 2. The characteristic matrix of the $j-$th layer of the stack is given by:

$$M_j = \begin{bmatrix} \cos\delta_{\mathrm{j}} & \frac{i}{\eta_{\mathrm{j}}}\sin\delta_{\mathrm{j}} \\ i\eta_{\mathrm{j}}\sin\delta_{\mathrm{j}} & \cos\delta_{\mathrm{j}} \end{bmatrix}, \quad j = 1, 2, 3\cdots, m$$

where

$$\delta_{\mathrm{j}} = \frac{2\pi N_{\mathrm{j}} d_{\mathrm{j}} \theta_{\mathrm{j}}}{\lambda},$$

is the phase thickness expressed in terms of the refractive index N_{j} and the physical thickness d_{j} of the layers, wavelength λ, and the angle of internal refraction θ_{j}. The optical admittances:

$$\eta_{\mathrm{j}} = \eta_{\mathrm{j}}\cos\theta_{\mathrm{j}} \text{ (TE pol.)}$$
$$\eta_{\mathrm{j}} = \frac{\eta_{\mathrm{j}}}{\cos\theta_{\mathrm{j}}} \text{ (TM pol.)}$$

depend on the polarization of light at non-normal incidence. The assumptions inherent in these simulations are that the interfaces between the adjacent layers is perfect (i.e. that there is no interfacial interdiffusion and no scattering loss).

The optical constants of the various materials, namely the complex refractive index $N = n - ik$ are derived from atomic scattering factors by Henke et. al. and were obtained from http://henke.lbl.gov/optical_constants/asf server at Berkeley [36]. The values of n and k for the materials used in this thesis were downloaded as functions of wavelength from 10 nm to 42 nm and as such the wavelength dependence of n and k is implicit in all calculations. The values of n and k at the wavelength of particular technological interest are listed in Table 1. The main aim of this thesis is to investigate the performance enhancement of the reflectors.

In order to reduce the effect on the reflectance response of the absorption losses, the thicknesses of the two components of the stack are adjusted slightly from the optical

path length of a quarter wavelength. The thickness of the high-absorption layer d_{h} is set slightly lower than that of the low absorption layer d_{l}. Thin film multilayer coatings greatly increase the reflection from surfaces in multi-element layer by making use of phase changes and the dependence of the reflectance on index of refraction. The idea behind multilayer coatings is that the creation of an interface by means of a thin film gives multiple reflected waves. The important property of a quarter-wave stacks is that a stack of quarter-wave layers of alternating refractive index high, low, high, low, ..., etc., has the reflection from every interface in phase. This gives constructive interference between every reflection, all the reflections add together and a quarter-wave stack of enough layers acts as a mirror at the wavelength λ. To maintain the phenomenon of standing wave in conventional high reflective mirror (quarter-wave stack), using the concept of ideal Bragg crystal, to achieve the result of standing wave and reduce the absorption in order to enhance the reflectance.

A quarter-wave layer is one which

$$N \times d = \lambda/4,$$

where N = refractive index of thin film, d = thickness of thin film, and λ = wavelength of light used. Hence, we made the total thickness of multilayer equal to the quarter-wave layer and adjusted the thickness of Mo and Si layer, and the reflectance results are listed in Table 4.1. As seen in Table 4.1, it is appear that the reflectance at 13.5-nm wavelength is coparison of the quarter-wave stack and fine-tuned Mo/Si multilayer structure which is used the way to adjust the layer thickness gradually. The fine-tuned Mo/Si multilayer structure is a 40 pair Mo/Si system ($d_{\mathrm{Mo}} = 3.4$ nm and $d_{\mathrm{Si}} = 3.6$ nm), yeilds a maximum reflectance around 71.25% of 13.5-nm wavelength, a peak reflectance of 72.34% at 13.60 nm, and the full-width-at-half-maximum (FWHM) is 0.758 nm.

Table 4.1: Reflectance versus individual thickness of Mo and Si layer.

	d_{Mo} (nm)	d_{Si} (nm)	Pair Number	$R_{\lambda\,=\,13.5\mathrm{nm}}$ (%)	R_{peak} (%) (λ_{peak})
quarter-wave stack	3.65	3.38	40	69.89	71.50 (13.62 nm)
fine-tuned Mo/Si	4.0	3.0	40	69.55	69.55 (13.50 nm)
fine-tuned Mo/Si	3.9	3.1	40	70.12	70.16 (13.52 nm)
fine-tuned Mo/Si	3.8	3.2	40	70.56	70.71 (13.53 nm)
fine-tuned Mo/Si	3.7	3.3	40	70.88	71.20 (13.55 nm)
fine-tuned Mo/Si	3.6	3.4	40	71.10	71.64 (13.57 nm)
fine-tuned Mo/Si	3.5	3.5	40	71.22	72.02 (13.58 nm)
fine-tuned Mo/Si	3.4	3.6	40	71.25	72.34 (13.60 nm)
fine-tuned Mo/Si	3.3	3.7	40	71.19	72.61 (13.61 nm)
fine-tuned Mo/Si	3.2	3.8	40	71.03	72.83 (13.62 nm)
fine-tuned Mo/Si	3.1	3.9	40	70.77	73.00 (13.64 nm)
fine-tuned Mo/Si	3.0	4.0	40	70.40	73.10 (13.65 nm)
fine-tuned Mo/Si	2.9	4.1	40	69.92	73.12 (13.67 nm)
fine-tuned Mo/Si	2.8	4.2	40	69.31	73.15 (13.68 nm)
fine-tuned Mo/Si	2.7	4.3	40	68.54	73.08 (13.69 nm)
fine-tuned Mo/Si	2.6	4.4	40	67.61	72.94 (13.70 nm)
fine-tuned Mo/Si	2.5	4.5	40	66.46	72.73 (13.71 nm)
fine-tuned Mo/Si	2.4	4.6	40	65.06	72.44 (13.72 nm)
fine-tuned Mo/Si	2.3	4.7	40	63.36	72.05 (13.73 nm)
fine-tuned Mo/Si	2.2	4.8	40	61.28	71.57 (13.74 nm)
fine-tuned Mo/Si	2.1	4.9	40	58.73	70.98 (13.75 nm)
fine-tuned Mo/Si	2.0	5.0	40	55.60	70.26 (13.76 nm)

The comparison spectral responses are shown in Figure 4-3. For the fine-tuned multilayer structure, the reflectance at 13.5-nm wavelength is increased from 69.89% to 71.25%; the peak reflectance is increased from 71.50% at 13.62 nm to 72.34% at 13.60 nm, too. In order to find the maximum reflectance, we also calculated the reflectance as the function of pair number in the multilayer and the result is shown in Figure 4-4. As a consequence, we could find the maximun reflectance with 54 pair fine-tuned Mo/Si multilayer structure (called Mo/Si ML structure) and still keeping the same value even though with more pairs. The spectral response for 54 pairs is then shown in Figure 4-5, which shows that the Mo/Si multilayer structure's reflectance at 13.5-nm wavelength is 71.65% and the peak reflectance is 72.91% at 13.61 nm and the FWHM is 0.710 nm. The detailed parameters of the Figure 4-4 are listed in Tables 4.2 and 4.3.

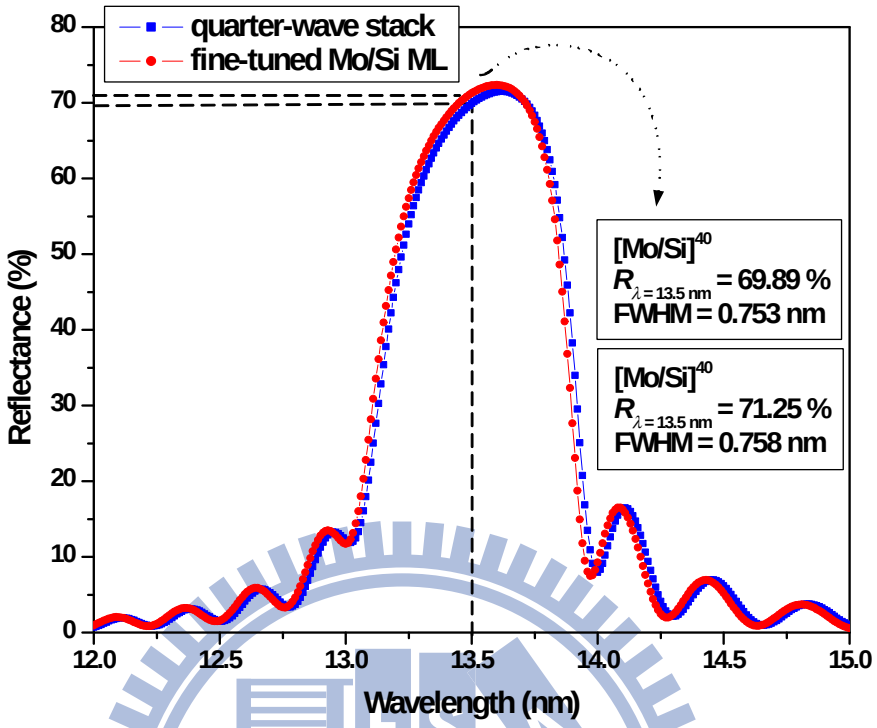

Figure 4-3: The spectral response for quarter-wave stack and fine-tuned Mo/Si ML structure.

Table 4.2: The maximum reflectance at 13.5-nm wavelength of fine-tuned Mo/Si ML structure with an increasing pair number.

Pair Number	R_{max} (%)	Pair Number	R_{max} (%)
40	71.25	49	71.59
41	71.32	50	71.61
42	71.37	51	71.62
43	71.42	52	71.63
44	71.46	53	71.64
45	71.50	54	71.65
46	71.52	55	71.65
47	71.55	56	71.65
48	71.57	57	71.65

Table 4.3: Parameters of three kinds of Si-based ML structures.

	d_{Mo} (nm)	d_{Si} (nm)	Pair Number	$R_{\lambda\,=\,13.5\ nm}$ (%)	R_{peak} (%)	FWHM (nm)
quarter-wave stack	3.65	3.38	40	69.89	71.50	0.753
fine-tuned Mo/Si ML	3.40	3.60	40	71.25	72.34	0.758
Mo/Si ML	3.40	3.60	54	71.65	72.91	0.710

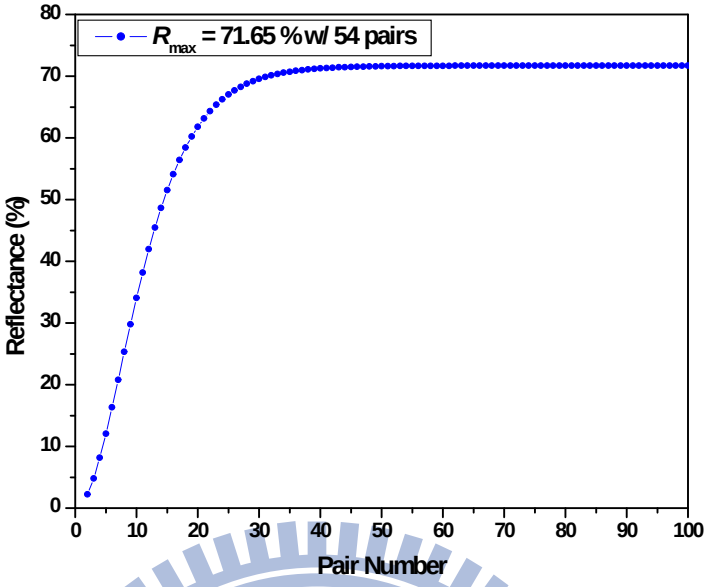

Figure 4-4: The reflectance versus the pair number for the fine-tuned Mo/Si ML structure.

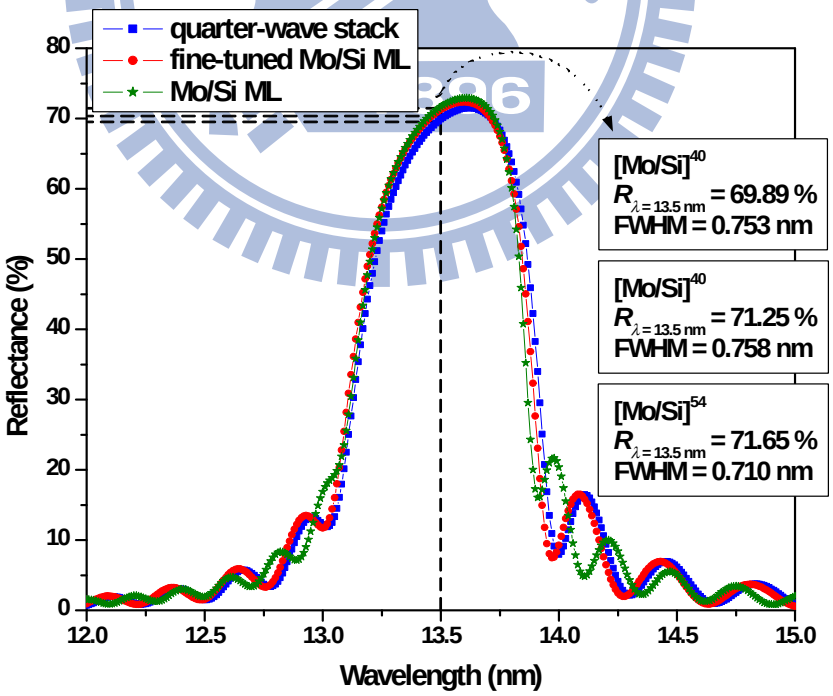

Figure 4-5: The spectral reflectance comparison of the quarter-wave stack, fine-tuned Mo/Si ML structure and Mo/Si ML structure.

4.3 Interface-Engineered Multilayer Structure

4.3.1 Design Consideration for an Interface-Engineered Multilayer Structure

The properties of Mo/Si multilayers are directly related to the structure of the interface. The interdiffusion processes and the roughness development significantly reduce the reflectance. One of the reasons for the disagreement between the achievable experimental reflectance and the theoretical analysis value for the Mo/Si multilayer system is the formation of intermixing zones at the interfaces. The major imperfections in the multilayers is the quality of the interface between the Mo and Si layers. Structural analysis revealed that these multilayers consist of layers of polycrystalline Mo and amorphous Si that are separated with interfacial regions of mixed composition, where the interface corresponding to Mo on Si is thicker than the interface corresponding to Si on Mo [45], [46]. Intermixing at interfaces can be decreased by using appropriate diffusion barriers. A number of studies have been performed to investigate the origin of Mo/Si intermixing and its dependence on the deposition parameters [47]. As a result, the intermixing regions have been minimized but not totally eliminated. That suggests that interlayer formation is an intrinsic property of the Mo/Si material and could present a fundamental barrier to achieve maximum optical performance. Since the interdiffusion layer formed between Mo and Si layers due to ion implantation or thermal diffusion may cause the deviation of the designed thickness and increase the absorption of the multilayers unexpectedly. Ru, B_4C, or C material will be used as the barrier layer material to constrain the interdiffusion layer and increase the thermal stability for the components [48], [49].

When EUV radiation illuminates on a multilayer structure, the superposition of the incident and reflected electromagnetic waves generates a standing wave field distribution in the multilayer stack, as illustrated in Figure 4-6 [48]. The structure is based on a periodic design and allows for a better spectral match of the emission distribution of the lithographic source (i.e., the stationary wave field is distributed to maximize interference of reflected components by multi-reflection inside each layer). Considering the amplitude of this standing wave as shown in Figure 4-6 the nodes and antinodes are at fixed positions of the multilayer stack. At the interface Mo-on-Si, the additional absorbing barrier layers will only weakly affect the electric field and the EUV reflectance. Hence any material that

is suitable as the barrier layer which is thin enough. From HRTEM micrographs [48] it can be concluded that for multilayers prepared by MSD the thicknesses of the intermixing zones are 1.2 nm for Mo-on-Si interface and 0.7 nm for Si-on-Mo interface. The aim of this section is to select promising materials and thicknesses of different barrier layers with respect to a highest possible EUV reflectance of the appropriate periodic configurations.

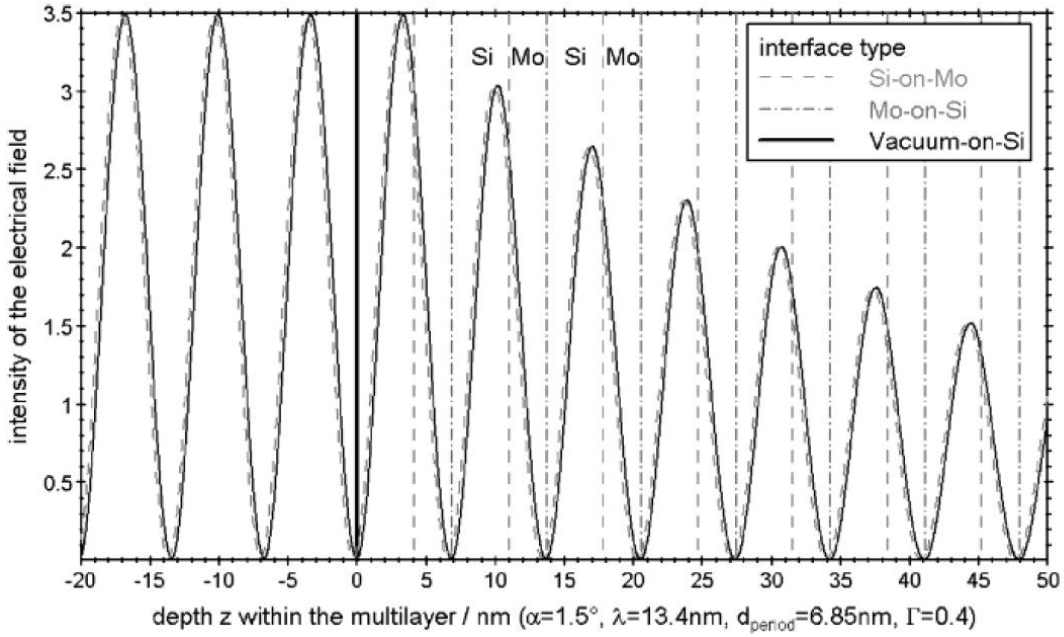

Figure 4-6: Distribution of the electrical field intensity within the Mo/Si multilayer structure in the case of maximum reflectance. The field intensity is high at the interfaces Si-on-Mo and low at the Mo-on-Si interfaces.

4.3.2 Reflectance Optimization with Different Barrier Layers in a Mo/Si Multilayer Structure

In extreme ultraviolet lithography, the multilayer reflectance and the thermal stability strongly depends on the diffusion barrier thicknesses. In this research, we have investigated to replace the original Mo/Si structure in one side layer or both layers by the barrier materials. Simulation results in Figure 4-7 show that regardless of the material as the barrier layer, the reflectance is over 70% for the barrier layer thickness $d \leq 1.2$ nm. Nevertheless, a final decision has to consider the suitability of the particular material as an diffusion and reaction between the individual layers of Mo and Si.

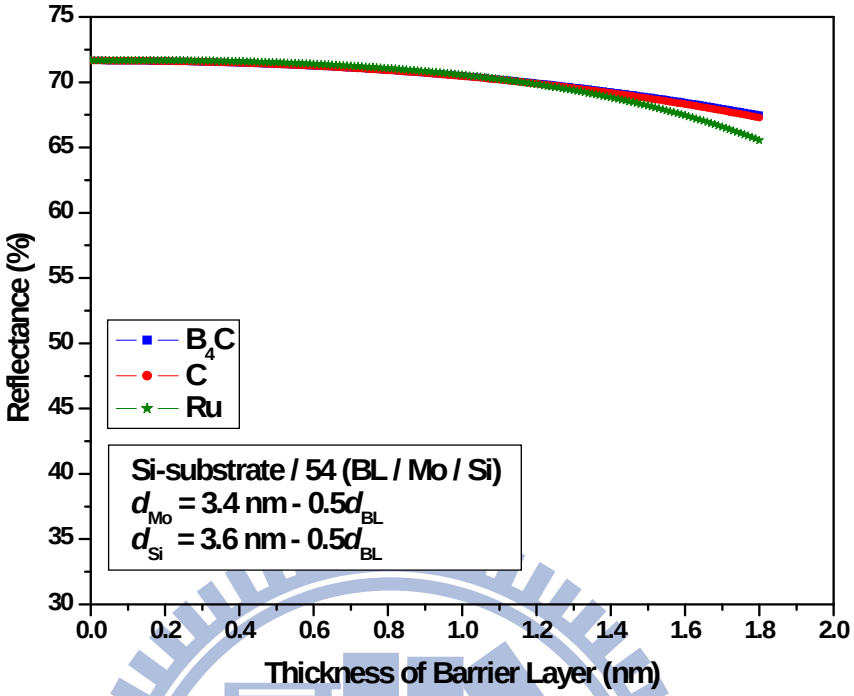

Figure 4-7: Calculations of EUV reflectance depending on the thickness of B_4C, C, and Ru barrier layers at the Mo-on-Si interface.

Consider the field intensity at the layer interfaces, the standing wave field has antinodes at Si-on-Mo interfaces and therefore the absorption of barrier layers at this stack position will strongly affect the EUV reflectance. We can do the similar calculation as Figure 4-7. From calculations, we can conclude that even materials with a lower EUV absorption like boroncarbide or carbon would cause a stronger loss to reflectance. Figure 4-8 shows the 13.5-nm reflectance obtained for multilayers that have three kinds of interlayer thicknesses in the range of 0.1−1.8 nm. Note that the variable barrier layer thickness, combined with a fixed pair thickness, results in an optical response that has a maximum in the reflectance curve at varying wavelengths in the range of 12−15 nm.

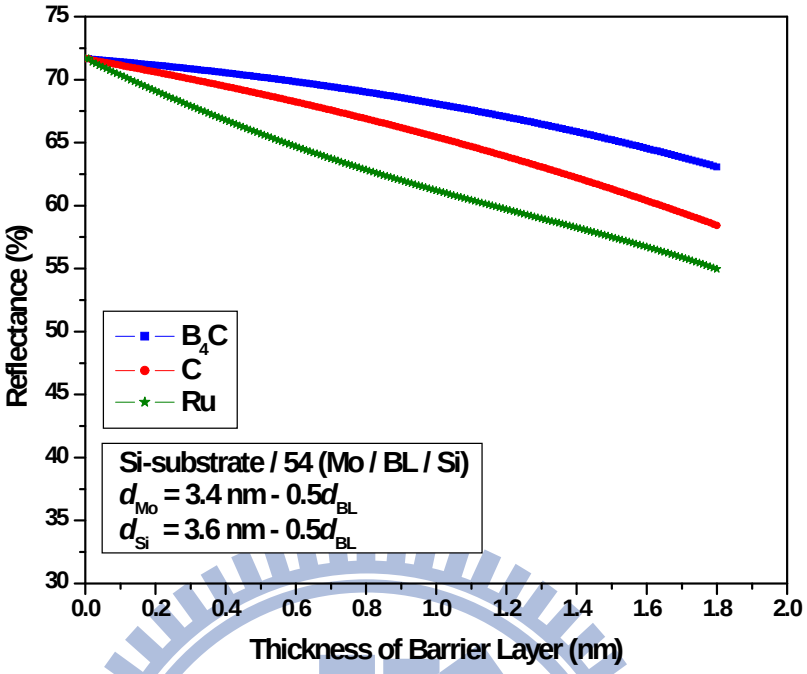

Figure 4-8: Calculations of EUV reflectance depending on the thicknesses of B_4C, C, and Ru barrier layers at the Si-on-Mo interface.

The case that the barrier layer replaces the original absorption layer (d_{Mo}) or spacer layer (d_{Si}) only are shown in Figures 4-9 to 4-12.

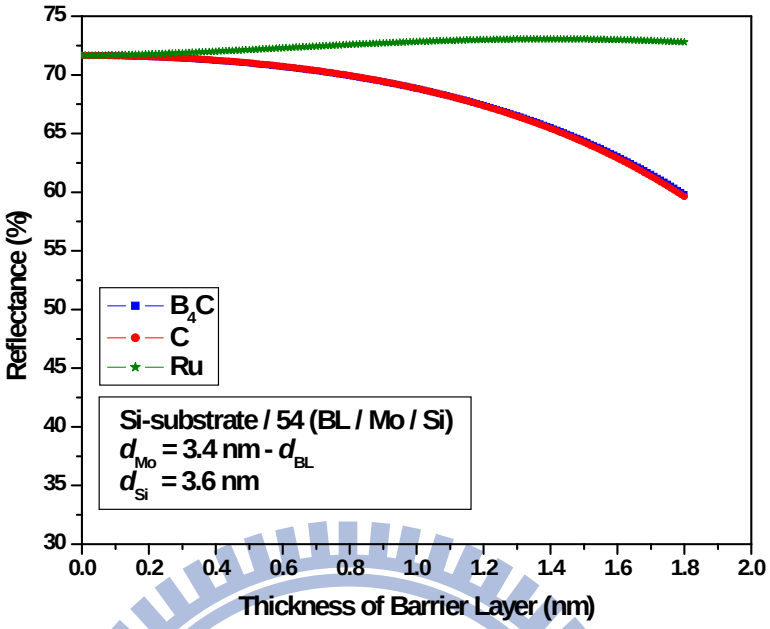

Figure 4-9: Calculations of EUV reflectance depending on the thickness of B_4C, C, and Ru barrier layers at the Mo-on-Si interface.

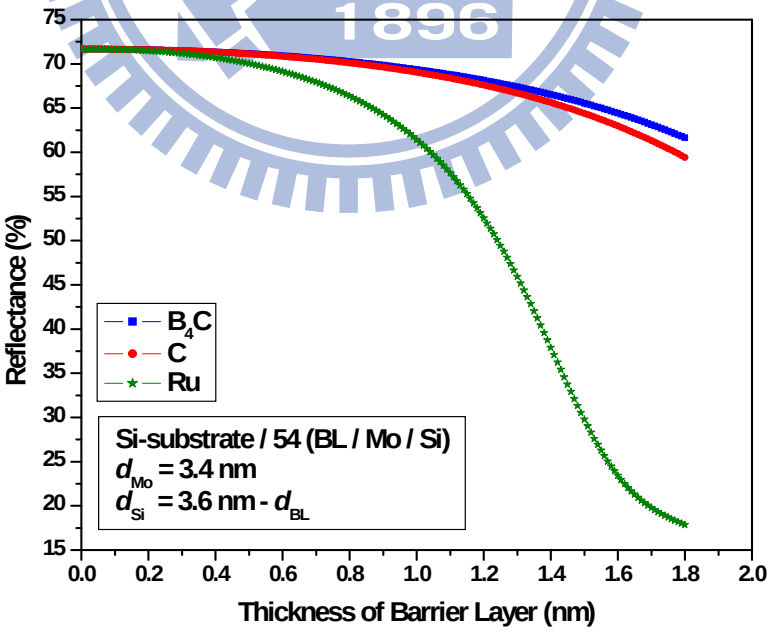

Figure 4-10: Calculations of EUV reflectance depending on the thickness of B_4C, C, and Ru barrier layers at the Mo-on-Si interface.

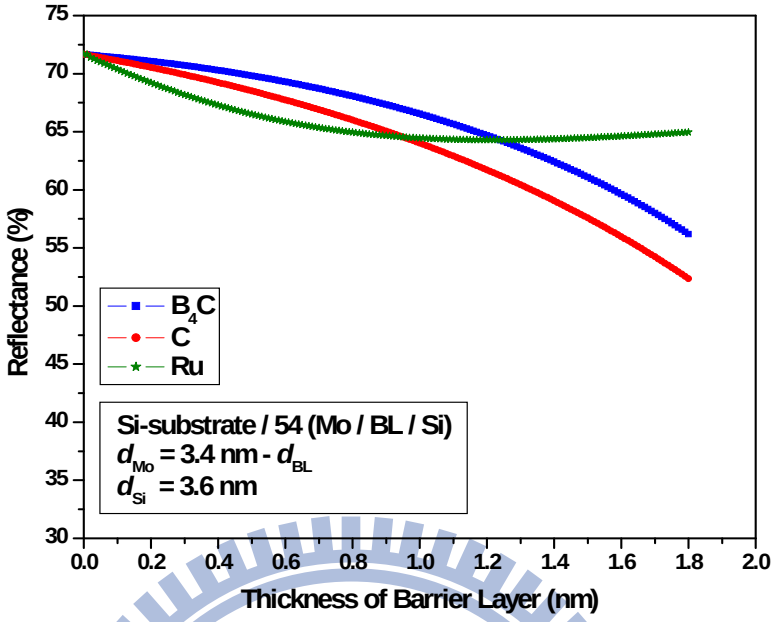

Figure 4-11: Calculations of EUV reflectance depending on the thicknesses of B_4C, C, and Ru barrier layers at the Si-on-Mo interface.

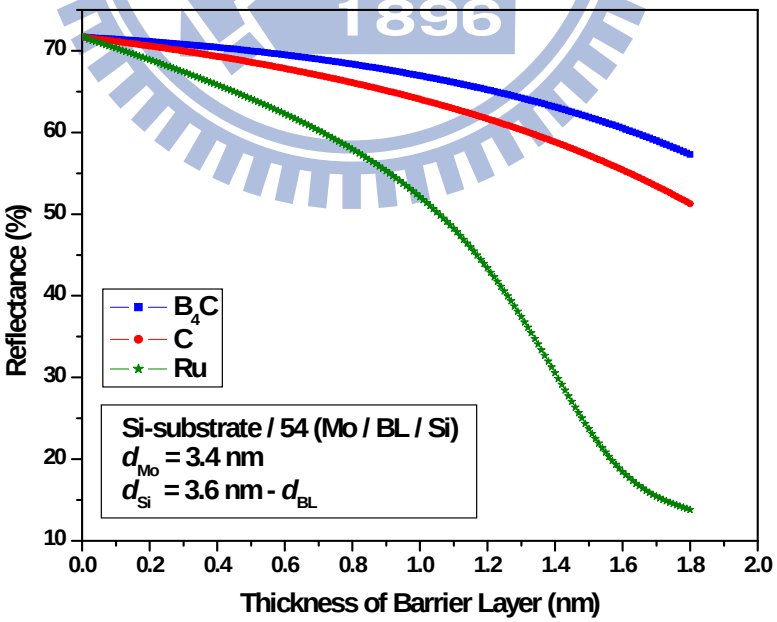

Figure 4-12: Calculations of EUV reflectance depending on the thicknesses of B_4C, C, and Ru barrier layers at the Si-on-Mo interface.

In this study, we used carbon, boroncarbide, and ruthenium as diffusion barrier layers for enhancement of the reflectance. The detailed parameters and the corresponding reflectance of interface-engineered ML structures are tabulated in Tables 4.4 - 4.9. Based on the simulation results of Tables 4.4 - 4.9, it was suggested that boroncarbide is more suitable as the barrier layer for applying at the Si-on-Mo interface. Similarly, it was suggested that ruthenium is more suitable as the barrier layer for applying at the Mo-on-Si interfaces.

Table 4.4: The detailed parameters of interface-engineered B_4C/Mo/Si ML structure at Mo-on-Si interface.

	d_{B_4C} (nm)	d_{Mo} (nm)	d_{Si} (nm)	$R_{\lambda\,=\,13.5\text{ nm}}$ (%)	R_{peak} (%) (λ_{peak})
B_4C/Mo/Si	0.2	3.4	3.6	31.51	72.86 (13.99 nm)
	0.2	3.2	3.6	71.53	73.56 (13.62 nm)
	0.2	3.4	3.4	71.59	72.52 (13.59 nm)
	0.2	3.3	3.5	71.60	72.87 (13.61 nm)

Table 4.5: The detailed parameters of interface-engineered C/Mo/Si ML structure at Mo-on-Si interface.

	d_C (nm)	d_{Mo} (nm)	d_{Si} (nm)	$R_{\lambda\,=\,13.5\text{ nm}}$ (%)	R_{peak} (%) (λ_{peak})
C/Mo/Si	0.2	3.4	3.6	31.76	72.83 (13.99 nm)
	0.2	3.2	3.6	71.54	73.14 (13.62 nm)
	0.2	3.4	3.4	71.58	72.49 (13.59 nm)
	0.2	3.3	3.5	71.61	72.84 (13.60 nm)

Table 4.6: The detailed parameters of interface-engineered Ru/Mo/Si ML structure at Mo-on-Si interface.

	d_{Ru} (nm)	d_{Mo} (nm)	d_{Si} (nm)	$R_{\lambda\,=\,13.5\text{ nm}}$ (%)	R_{peak} (%) (λ_{peak})
Ru/Mo/Si	0.2	3.4	3.6	39.31	72.32 (13.96 nm)
	0.2	3.2	3.6	71.76	72.72 (13.59 nm)
	0.2	3.4	3.4	71.47	71.85 (13.57 nm)
	0.2	3.3	3.5	71.66	72.32 (13.57 nm)
	1.4	2.0	3.6	73.04	73.74 (13.58 nm)

Table 4.7: The detailed parameters of interface-engineered Mo/B_4C/Si ML structure at Si-on-Mo interface.

	d_{Mo} (nm)	d_{B_4C} (nm)	d_{Si} (nm)	$R_{\lambda\,=\,13.5\text{ nm}}$ (%)	R_{peak} (%) (λ_{peak})
Mo/B_4C/Si	3.4	0.2	3.6	31.31	72.42 (13.99 nm)
	3.2	0.2	3.6	71.09	72.71 (13.62 nm)
	3.4	0.2	3.4	71.14	72.08 (13.59 nm)
	3.3	0.2	3.5	71.16	72.42 (13.61 nm)

Table 4.8: The detailed parameters of interface-engineered Mo/C/Si ML structure at Si-on-Mo interface.

	d_{Mo} (nm)	d_{C} (nm)	d_{Si} (nm)	$R_{\lambda\,=\,13.5\text{ nm}}$ (%)	R_{peak} (%) (λ_{peak})
Mo/C/Si	3.4	0.2	3.6	31.30	71.84 (13.99 nm)
	3.2	0.2	3.6	70.53	72.12 (13.62 nm)
	3.4	0.2	3.4	70.57	71.47 (13.59 nm)
	3.3	0.2	3.5	70.60	71.81 (13.60 nm)

Table 4.9: The detailed parameters of interface-engineered Mo/Ru/Si ML structure at Si-on-Mo interface.

	d_{Mo} (nm)	d_{Ru} (nm)	d_{Si} (nm)	$R_{\lambda\,=\,13.5\text{ nm}}$ (%)	R_{peak} (%) (λ_{peak})
Mo/Ru/Si	3.4	0.2	3.6	37.90	69.82 (13.96 nm)
	3.2	0.2	3.6	69.22	70.16 (13.59 nm)
	3.4	0.2	3.4	68.90	69.30 (13.56 nm)
	3.3	0.2	3.5	69.10	69.75 (13.57 nm)

Making these values was chosen to obtain good agreement between simulations, we have design a fine structure Ru/Mo/B_4C/Si. Calculations of the thickness with different barrier layers at every interface are listed in Table 4.10 as follows.

Table 4.10: The detailed parameters of interface-engineered Ru/Mo/B_4C/Si ML structure.

	d_{Ru} (nm)	d_{Mo} (nm)	d_{B_4C} (nm)	d_{Si} (nm)	$R_{\lambda\ =\ 13.5\ nm}$ (%)	R_{peak} (%) (λ_{peak})
Ru/Mo/B_4C/Si	0.2	3.4	0.2	3.6	‹10%	71.87 (14.35 nm)
	0.2	3.2	0.2	3.4	71.18	71.83 (13.57 nm)
	0.2	3.0	0.2	3.6	71.28	72.58 (13.61 nm)
	0.2	3.4	0.2	3.2	70.68	70.88 (13.54 nm)
	1.4	3.4	0.2	3.6	‹1%	‹3%
	1.4	2.6	0.2	2.8	68.38	69.26 (13.43 nm)
	1.4	1.8	0.2	3.6	72.61	73.64 (13.60 nm)
	1.4	3.4	0.2	2.0	29.69	59.64 (13.25 nm)
	1.4	2.0	0.2	3.6	53.86	73.29 (13.96 nm)

Based on Table 4.6, by choosing d_{Ru} = 1.4 nm, d_{Mo} = 2.0 nm, and d_{Si} = 3.6 nm, we could achieve a higher reflectance 73.04% at 13.5-nm wavelength, a peak reflectance 73.74% at 13.58 nm with Ru/Mo/Si multilayer structure, and a FWHM of 0.829 nm as shown in Figure 4-13. Likewise, based on Table 4.7 with d_{B_4C} = 0.2 nm, d_{Mo} = 3.3 nm, and d_{Si} = 3.5 nm, we could achieve a higher reflectance 71.16% at 13.5-nm wavelength, a peak reflectance 72.42% at 13.61 nm with Mo/B_4C/Si multilayer structure, and a FWHM of 0.708 nm as shown in Figure 4-13. Considering the practical process and using ruthenium and boron carbide as barrier layers at all interfaces as shown in Table 4.10 with d_{Ru} = 1.4 nm, d_{B_4C} = 0.2 nm, d_{Mo} = 1.8 nm, and d_{Si} = 3.6 nm, we could achieve a higher reflectance 72.61% at 13.5-nm wavelength, a peak reflectance 73.64% at 13.60 nm with Ru/Mo/B_4C/Si multilayer structure, and a FWHM of 0.837 nm as shown in Figure 4-13. These spectral reflectance comparison are all shown in Figure 4-13. We have also investigated reflectance dependency on each thin-film thickness, and the results are listed in Tables 4.11 - 4.15. With d_{Ru} = 1.4 nm, d_{B_4C} = 0.2 nm, d_{Mo} = 1.9 nm, and d_{Si} = 3.5 nm, we have achieved a higher reflectance 72.62% at 13.5-nm wavelength, a peak reflectance 73.30% at 13.58 nm with Ru/Mo/B_4C/Si multilayer structure, and a FWHM of 0.828 nm as shown in Figure 4-14. The detailed parameters of ML structures are listed in Tables 4.16 and 4.17. Although the higher reflectance seems to be Ru/Mo/Si multilayer structure, we should consider the experimental process to choose the useful Ru/Mo/B_4C/Si multilayer structure.

Table 4.11: The detailed parameters of interface-engineered Ru/Mo/B_4C/Si ML structure with thickness dependent.

	d_{Ru} (nm)	d_{Mo} (nm)	d_{B_4C} (nm)	d_{Si} (nm)	$R_{\lambda\ =\ 13.5\ nm}$ (%)	R_{peak} (%) (λ_{peak})
Ru/Mo/B_4C/Si	1.2	1.8	0.2	3.8	72.29	74.12 (13.63 nm)
	1.2	1.9	0.2	3.7	72.48	73.87 (13.61 nm)
	1.2	2.0	0.2	3.6	72.57	73.56 (13.59 nm)
	1.2	2.1	0.2	3.5	72.55	73.20 (13.57 nm)

Table 4.12: The detailed parameters of interface-engineered Ru/Mo/B_4C/Si ML structure with thickness dependent.

	d_{Ru} (nm)	d_{Mo} (nm)	d_{B_4C} (nm)	d_{Si} (nm)	$R_{\lambda\ =\ 13.5\ nm}$ (%)	R_{peak} (%) (λ_{peak})
Ru/Mo/B_4C/Si	1.3	1.8	0.2	3.7	72.50	73.91 (13.62 nm)
	1.3	1.9	0.2	3.6	72.60	73.61 (13.59 nm)
	1.3	2.0	0.2	3.5	72.60	73.27 (13.58 nm)
	1.3	2.1	0.2	3.4	72.48	72.86 (13.55 nm)

Table 4.13: The detailed parameters of interface-engineered Ru/Mo/B_4C/Si ML structure with thickness dependent.

	d_{Ru} (nm)	d_{Mo} (nm)	d_{B_4C} (nm)	d_{Si} (nm)	$R_{\lambda\ =\ 13.5\ nm}$ (%)	R_{peak} (%) (λ_{peak})
Ru/Mo/B_4C/Si	1.4	1.7	0.2	3.7	72.49	73.91 (13.61 nm)
	1.4	1.8	0.2	3.6	72.61	73.64 (13.60 nm)
	1.4	1.9	0.2	3.5	72.62	73.30 (13.58 nm)
	1.4	2.0	0.2	3.4	72.51	72.91 (13.56 nm)

Table 4.14: The detailed parameters of interface-engineered Ru/Mo/B_4C/Si ML structure with thickness dependent.

	d_{Ru} (nm)	d_{Mo} (nm)	d_{B_4C} (nm)	d_{Si} (nm)	$R_{\lambda\ =\ 13.5\ nm}$ (%)	R_{peak} (%) (λ_{peak})
Ru/Mo/B_4C/Si	1.5	1.6	0.2	3.7	72.45	73.88 (13.62 nm)
	1.5	1.7	0.2	3.6	72.58	73.62 (13.60 nm)
	1.5	1.8	0.2	3.5	72.61	73.31 (13.58 nm)
	1.5	1.9	0.2	3.4	72.52	72.93 (13.56 nm)

Table 4.15: The detailed parameters of interface-engineered Ru/Mo/B_4C/Si ML structure with thickness dependent.

	d_{Ru} (nm)	d_{Mo} (nm)	d_{B_4C} (nm)	d_{Si} (nm)	$R_{\lambda\ =\ 13.5\ nm}$ (%)	R_{peak} (%) (λ_{peak})
Ru/Mo/B_4C/Si	1.6	1.5	0.2	3.7	72.38	73.81 (13.62 nm)
	1.6	1.6	0.2	3.6	72.52	73.57 (13.60 nm)
	1.6	1.7	0.2	3.5	72.57	73.28 (13.58 nm)
	1.6	1.8	0.2	3.4	72.50	72.92 (13.56 nm)

Table 4.16: The detailed parameters of interface-engineered Ru/Mo/Si, Mo/B_4C/Si, and Ru/Mo/B_4C/Si ML structures.

	d_{BL} (nm)		d_{Mo} (nm)	d_{Si} (nm)	$R_{\lambda\ =\ 13.5\ nm}$ (%)	R_{peak} (%)
Ru/Mo/Si	d_{Ru} = 1.4		2.0	3.6	73.04	73.74 (13.58nm)
Mo/B_4C/Si	d_{B_4C} = 0.2		3.3	3.5	71.16	72.42 (13.61nm)
Ru/Mo/B_4C/Si	d_{Ru} = 1.4	d_{B_4C} = 0.2	1.8	3.6	72.61	73.64 (13.60nm)

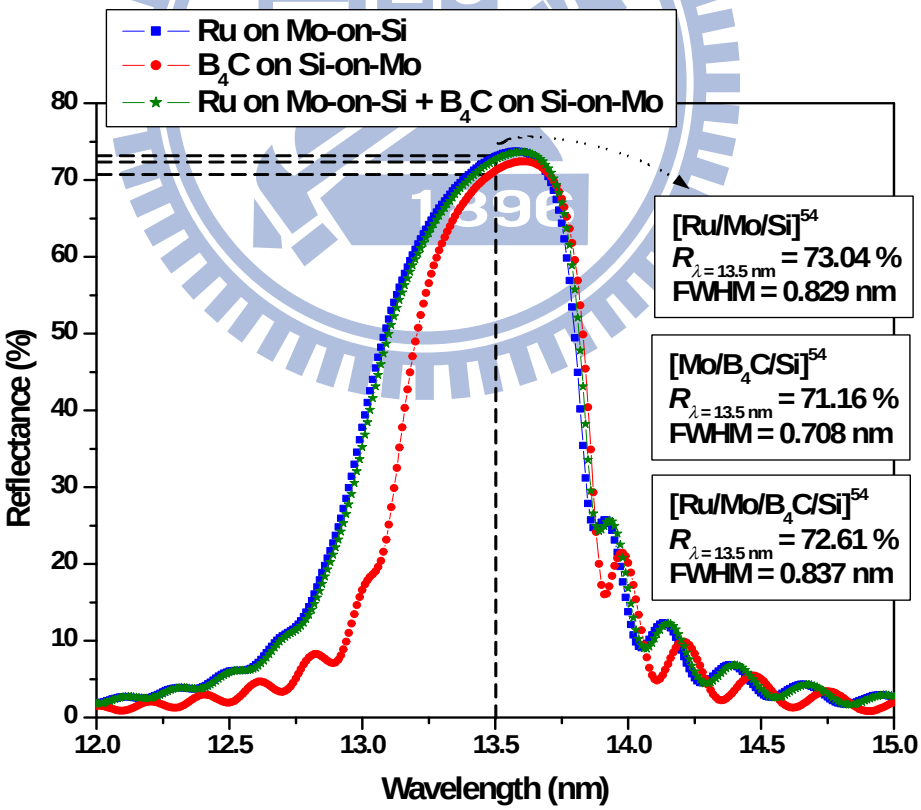

Figure 4-13: The spectral reflectance comparison of the Ru/Mo/Si ML structure, Mo/B_4C/Si ML structure, and Ru/Mo/B_4C/Si ML structure.

Table 4.17: The detailed parameters of interface-engineered Mo/Si ML structure and Ru/Mo/B_4C/Si ML structure.

	d_{BL}(nm)		d_{Mo}(nm)	d_{Si}(nm)	$R_{\lambda\,=\,13.5\ \mathrm{nm}}$ (%)	R_{peak} (%)
Mo/Si	0		3.4	3.6	71.65	72.91 (13.61 nm)
Ru/Mo/B_4C/Si	$d_{Ru} = 1.4$	$d_{B_4C} = 0.2$	1.9	3.5	72.62	73.30 (13.58 nm)

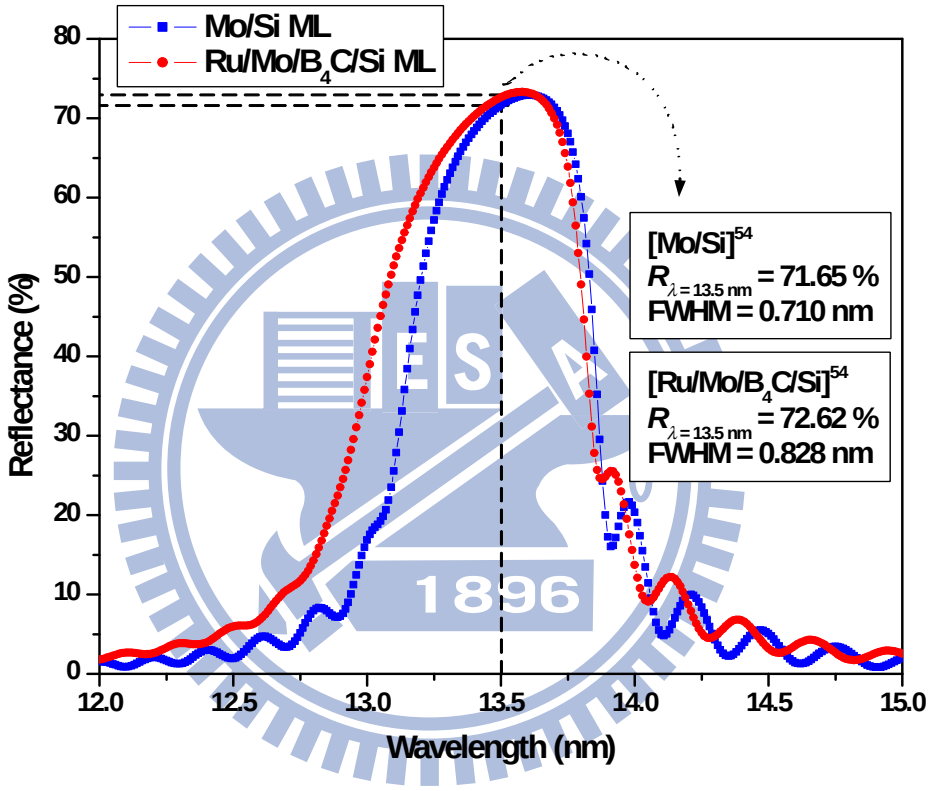

Figure 4-14: The spectral reflectance comparison of the Mo/Si ML structure and Ru/Mo/B_4C/Si ML structure.

4.4 Capping Layer to Avoid the Oxidation

4.4.1 Design Consideration with a Capping Layer

To determine the suitability of candidate materials for the capping layer, we first extracted information on densities (ρ), delta (δ), beta (β), and attenuation lengths at 13.5 nm (91.84 eV) for pure elements ($Z = 1 - 92$) and compound materials from the CXRO webpage [36]. Using CXRO data, we calculated the reflectance of a 54 bilayer Mo/Si multilayer structure with a period thickness of 7.0 nm (Si layer thickness = 3.6 nm and Mo layer thickness = 3.4 nm). The calculation assumed a perfect multilayer structure (no roughness, interdiffusion, or surface oxide), and it was performed for normal incidence angle, assuming that the substrate was a Si wafer with 0.1 nm surface roughness. One of the major imperfections in the multilayers that reduces the reflectance is the formation of the surface oxide. It is impossible to completely avoid it, because the multilayers get exposed to air. However, choosing a material to terminate the multilayer that forms a thinner, less absorbing surface oxide than Si may mitigate this effect. Interestingly, the silicide layer thicknesses are interface-dependent. For example, the silicide thickness of the Mo-on-Si interface is at least two times thicker than that of the Si-on-Mo interface. The appearance of the asymmetry in the silicide thickness is associated with a phase transition from amorphous to crystalline structure in Mo layers. Roughness of interfaces is yet another imperfection that lowers the multilayer reflectance. However, some studies suggest that interfacial roughness is negligible for optimized sputtering conditions [52]. Fortunately, in an optimized EUV multilayer the Mo thickness is well above that transition. Approaching to improve the reflectance of EUV multilayers was to engineer the interfaces to minimize the silicide formation. The idea is to limit the interdiffusion of Mo and Si by using a third material as a diffusion barrier that is light-transparent. This idea was recently used by other authors to improve the thermal stability of the multilayers, but always at the expense of slightly lower reflectance [42], [48], [51]. In the following, we will call such interface-engineered multilayers as (standard) Mo/Si multilayers structure. The multilayers with Mo and Si layers separated with thin barrier layers will be designed as a useful structure to be applied for EUV lithographic system.

Since the maximum reflectance peak did not always coincide with 13.5-nm wavelength due to different optical constants of the capping layers, it has been reported three

numbers in tables in Appendix C [51]: reflectance at 13.5 nm ($R_{\lambda\,=\,13.5\text{ nm}}$), the peak wavelength corresponding to the maximum reflectance ($\lambda_{\max}$), and the maximum value of reflectance at peak wavelength ($R_{\max}$). The maximum peak reflectance and the 13.5 nm reflectance are typically off by only ± 0.1 nm and the difference in reflectance very rarely exceeds 1%, which is much less than the uncertainties in the optical constant values. It is straightforward to design a multilayer where the maximum peak reflectance and the reflectance at 13.5 nm coincide by adjusting the capping layer thickness. To be considered as the capable capping layer, elemental materials were allowed to cause a drop in reflectance for the entire film stack of 1% or less, and 2% or less was allowed for compounds. The different criteria for elements v.s. compounds was used because of the relatively larger uncertainties in the calculated (v.s. experimentally determined) optical constants for compounds [44]. Reflectance calculation results for non-gaseous elemental and compound materials that meet these criteria are summarized in Tables [51], respectively. Negative values for $\triangle R = R(\text{Si}) - R(\text{max})$ are observed for some materials and indicate that the addition of a capping layer of that thickness results in a slight increase in reflectance. Complete results of the reflectance calculations for all of the materials under consideration are given in the Appendix [51].

Accordingly, the decision that if a class of materials appeared promising from a surface chemistry perspective, then those materials would be choosen as candidates from the viewpoint of the other gating criteria even if the optical performance were unknown. Of course, if the material appears promising in all other aspects, it is surely recommended to fabricate films to measure its optical constants through experiment and determine whether the material is indeed worth a full capping layer development.

4.4.2 Material Selection for the Capping Layer

Based on the optical constants data and discussed in the previous section, we can identify potential candidate materials for capping layers. First, considering the stability of the films when exposed to atmospheric air. The films will be deposited in vacuum, but at some situation they will be inevitable to be exposed to air with some moisture contents. Lots of materials with favorable optical properties fail at this first stage, due to rapid oxidation, hydroxide, or carbonate formation which can compromise the film's opticals. Even films that are not completely oxidized will still be affected by air exposure. Film

microstructure will affect the reactivity. Then, considering the films' reactivity during exposure to background vacuum gases (mainly H_2, H_2O, CO, CO_2, and C_nH_{2n+2}). Including deposition of carbon, reactions would accelerate growth of oxides, hydroxides, carbides, and oxycarbides, etc. And the effects of EUV radiation-induced processes are important too. The radiation-induced dissociation of adsorbed background gases and the reactivity of atomic and radical fragments are affected most strongly by indirect processes (i.e., low energy secondary electrons released from the substrate during irradiation by EUV photons). Ultimately, many-sided mitigation should be considered. A related major concerns possible removal of built-up carbon layers, or reduction of oxides. Atomic hydrogen has been shown to be effective for cleaning both C and O from certain surfaces [51].

The following non-gaseous elements are considered; they are identified by their row of the periodic table as shown in Figure 4-15 [51]. All of these have favorable optical properties as capping layers when covering Si as the top layer.

H																	He
Li	Be											B	C	N	O	F	Ne
Na	Mg											Al	Si	P	S	Cl	Ar
K	Ca	Sc	Ti	V	Cr	Mn	Fe	Co	Ni	Cu	Zn	Ga	Ge	As	Se	Br	Kr
Rb	Sr	Y	Zr	Nb	Mo	Tc	Ru	Rh	Pd	Ag	Cd	In	Sn	Sb	Te	I	Xe
Cs	Ba	La	Hf	Ta	W	Re	Os	Ir	Pt	Au	Hg	Tl	Pb	Bi	Po	At	Rn
Fr	Ra	Ac	Rf	Db	Sg	Bh	Hs	Mt									

Ce	Pr	Nd	Pm	Sm	Eu	Gd	Tb	Dy	Ho	Er	Tm	Yb	Lu
Th	Pa	U	Np	Pu	Am	Cm	Bk	Cf	Es	Fm	Md	No	Lr

Figure 4-15: All non-shaded elements in the periodic table have good optical properties.

2^{nd} row: Li, Be, B, C

3^{rd} row: Si, P, S

4^{th}row: K, Ca, Sc, Ti, V

5^{th} row: Rb, Sr, Y, Zr, Nb, Mo, Tc, Ru, Rh, Pd

6^{th} row and Rare Earths: Ba, Pt, La, Ce, Pr, Nd, Pm, Sm, Eu

Actinides: U

Ru, Rh, Ir

Three metals Ru, Rh, and Ir are attractive so far because thin films with these materials deposited in vacuum can undergo air exposure and remain metallic. In addition, they do not react significantly with H_2O vapor. Ru forms ultrathin oxide films with (relatively) low heats of formation per O atom. Bulk oxidation of Ru does not occur spontaneously upon exposure to O-containing gases at 300 K, and the oxygen-covered surface can be reduced by H atoms [51]. Many aspects of the surface chemistry of Ru in EUV applications have been discussed by previous workers [53]. Rh and Pd have many of the benefits of Ru and may be even better than Ru in some ways: they have weaker interaction with water vapor, more weakly bonded oxide than Ru, and are easily reduced by gaseous hydrogen with gentle heating. The previous discussion does not take into account the growth mode of elemental materials (metals) on multilayers, which may impact the capping layer. It is important to understand whether the growth proceeds more-or-less layer-by-layer, or in a form of cluster (island) growth. For example, a continuous and stable 2-nm Ru film can be sputter-deposited onto a Mo/Si multilayer mirror, but films of certain metals (e.g., Pd, Au) grow as discontinuous 3D islands under the same deposition conditions. It is also critical to understand how the film morphology is affected by subsequent reaction with background gases.

Based on the above information and all review papers mentioned, and with little knowledge of film growth considerations, here are the "best bets" from a "surface chemistry" point of view [51]. If the following materials can be deposited on the terminating Si layer and remain stoichiometric, smooth and continuous, and if pinholes and grain boundaries are minimal, they may be worth considering for further development of a research and characterization strategy.

Best material choice

Elemental Materials: Ru, Rh

4.4.3 Reflectance Optimization for the Interface-Engineered Multilayer Structure with a Capping Layer

The reflectance of EUV multilayer structures can be degraded significantly by hydrocarbon contamination or by the growth of an oxide layer on the top surface due to environmental contaminants. Contamination by heavier hydrocarbons is the most problematic, as light hydrocarbons can be removed by heating the optics up to about 30 degree. The oxidation depends on the interaction between EUV photons and the multilayer material. EUV photons cause primary electron emission by the photo-electric effect and the primary electrons in turn generate secondary electrons by interaction with the atoms of the multilayer materials. The mean free path of secondary electrons in the materials is only a few nanometers, so only those electrons generated in the top few layers [39] can reach the vacuum. To overcome the problem of surface contamination and oxidation, the use of a protective capping layer has been investigated [54]. It is crucial to find a capping-layer material that is oxidation-resistant, forms a sharp and stable interface with the material underneath, and has good optical properties in the EUV region.

The typical top layer is Si, and this oxidizes very easily, especially during EUV light exposure. However, this additional oxide will reduce the mask blank reflectance due to a higher absorption of EUV light. We simulated the performances of the multilayer structure capped with Ru, Rh, Pt, and native Si oxide as well. In Figure 4-16, the results of simulations show a higher reflectance in the case of multilayers containing Ru or Rh capping layer, the opposite is for multilayer containing SiO_2 or Pt capping layer (Unfortunately, it is generally recognized that an SiO_2 capping layer is not a suitable solution for a photolithographic apparatus due to poor resistence to oxidation). Even though a ultra-thin Ru or Rh capping layer can slightly increases reflectance, while a thicker film can result in a fast drop of reflectance. There is reasonable for Ru has been chosen as a capping layer since it is known to be oxidation-resistant. From the results, Ru layer of 1.9-nm thickness can be suggested as a capping layer with interface-engineered Mo/Si multilayer structure; however, the sufficient thickness to be oxidation-resistant is around 2-3 nm in the lithography process. Hence, we chose the thin Ru layer of 2-nm thickness as a capping layer with interface-engineered Mo/Si multilayer structure.

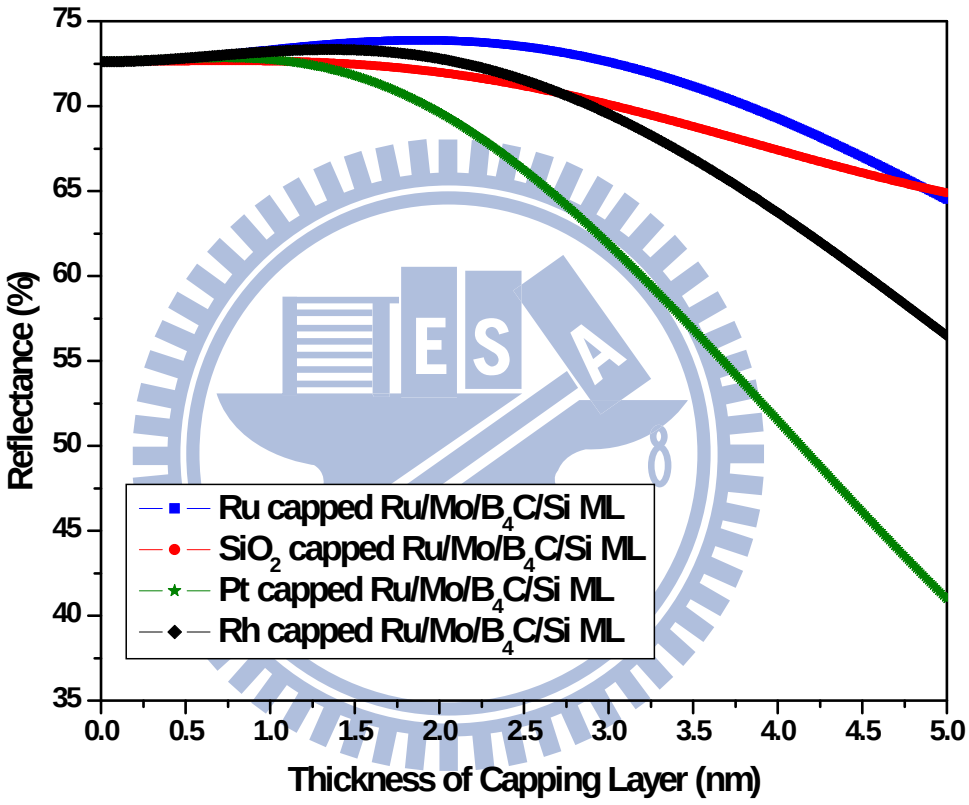

Figure 4-16: The reflectance versus the capping thickness with different kinds of materials on Ru/Mo/B_4C/Si ML structure.

A interface-engineered Mo/Si multilayer structure with 54 pairs, a period thickness of 7.0 nm, and a 2.0-nm-thick Ru capping layer. Considering the exposure light is on 13.5-nm wavelength, the reflectance is 73.86% with Ru/Mo/B_4C/Si multilayer structure, and a FWHM of 0.845 nm. Figure 4-17 shows the reflectance versus the thickness of the capping layer and the results shows that there is an optimized thickness. And the detailed parameters of different interface-engineered multilayer structures with a Ru capping layer are listed in Table 4.18 and the spectral responses are shown in Figure 4-18. Although the highest reflectance seems to be 1.9-nm-thick Ru capping layer, we still chose a 2.0-nm Ru capping thickness for considering practical process. Finally, we have a multilayer structrure with $d_{\mathrm{Ru}} = 1.4$ nm, $d_{\mathrm{B_4C}} = 0.2$ nm, $d_{\mathrm{Mo}} = 1.9$ nm and $d_{\mathrm{Si}} = 3.5$ nm with 2.0-nm Ru as a capping layer to achieve a better reflectance 73.86% at 13.5-nm wavelength, a peak reflectance 74.42% at 13.57 nm, and a FWHM of 0.845 nm.

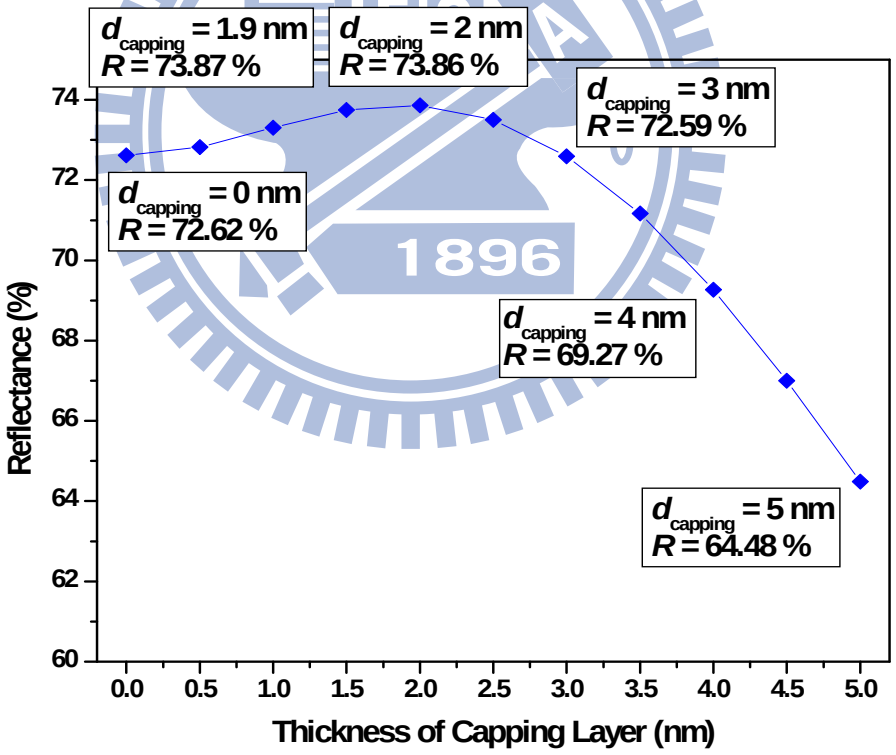

Figure 4-17: The reflectance versus the capping thickness with the Ru/Mo/B_4C/Si ML structure and Ru as the capping material.

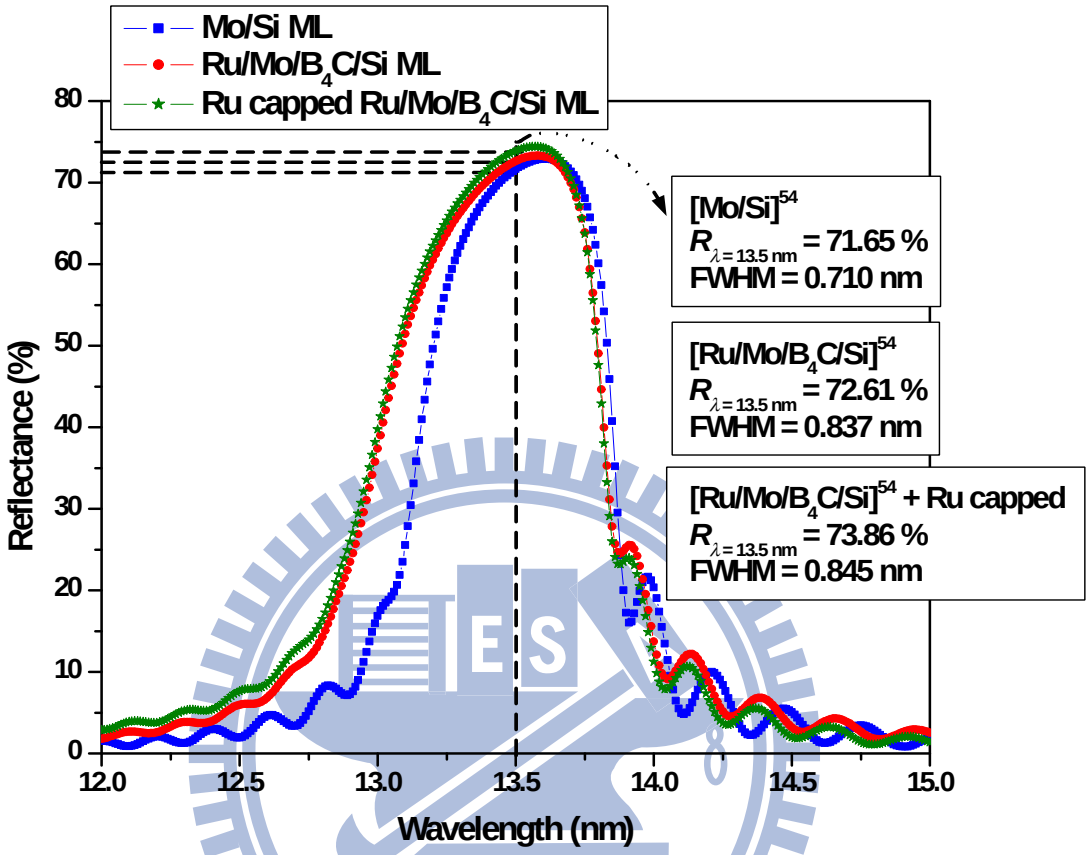

Figure 4-18: The spectral reflectance comparison for Mo/Si ML structure, Ru/Mo/B_4C/Si ML structure, and Ru/Mo/B_4C/Si ML structure with a 2.0-nm Ru as a capping layer.

Table 4.18: The detailed parameters of Mo/Si ML structure, Ru/Mo/B_4C/Si ML structure, and Ru/Mo/B_4C/Si ML structure with a 2.0-nm Ru as a capping layer.

	d_{cap} (nm)	d_{BL} (nm)		d_{Mo} (nm)	d_{Si} (nm)	$R_{\lambda\ =\ 13.5\ nm}$ (%)
Mo/Si ML	0	0		3.4	3.6	71.65
Ru/Mo/B_4C/Si ML	0	$d_{Ru} = 1.4$	$d_{B_4C} = 0.2$	1.9	3.5	72.62
Ru capped Ru/Mo/B_4C/Si ML	2.0	$d_{Ru} = 1.4$	$d_{B_4C} = 0.2$	1.9	3.5	73.86

Chapter 5

Conclusion

In our investigations, we have designed and simulated the characteristics of multilayer, interface-engineered multilayer structure, and with a capping layer applied for reflectance improvement of multilayer mirrors and masks for extreme-ultraviolet lithography.

The success of extreme-ultraviolet lithography is mostly dependent on the performance and stability of multilayer coatings. These multilayers need to maintain a high reflectance in a realistic lithography tool environment. The optics used to reflect and focus 13.5-nm wavelength ($\sim$ 92 eV) EUV radiation are Mo/Si multilayer mirrors which function in 10^{-5} Pa vacuum of EUVL exposure tools. We have developed a multilayer structure using interface-engineering in which the Mo and Si layers are separated with low-atomic-weight interlayers (boron carbide) at Si-on-Mo interface and high absorption material (ruthenium) at Mo-on-Si interface, respectively. In addition we have also investigated different capping layers to avoid reflectance degrading in the presence of EUV light and water vapor. In this study we addressed the reflectance loss due to interdiffusion and oxidation; the best design was observed on Ru-capped multilayers with a Ru/Mo/B_4C/Si ML structure between the Ru capping layer and the Si substrate. Longer exposures in different environments are necessary to test lifetime stability over many years. Coating the multilayers with thin (2 nm) capping layer films can reduce build-up of contamination (mostly oxides, carbon films).

In the design, we first made the total thickness of multilayer to satisfy the quarter-wave stack condition and then adjusted the thickness of Mo and Si layer. For the original quarter-wave stack the reflectance at 13.5-nm wavelength is 69.89%, the peak reflectance is 71.50% at 13.62 nm, and the full-width-at-half-maximum (FWHM) is 0.753 nm. The

fine-tuned multilayer stack for a 40 pair Mo/Si system ($d_{\mathrm{Mo}} = 3.4$ nm and $d_{\mathrm{Si}} = 3.6$ nm) yeilds a maximum reflectance around 71.25 % at 13.5-nm wavelength, a peak reflectance of 72.34% at 13.60 nm, and a FWHM of 0.758 nm. Based on the structure, we also investigated the influence of the pair number, then we could find the maximum reflectance with 54 pair fine-tuned Mo/Si multilayer structure (called Mo/Si ML structure) and still keeping the same reflectance even with more pairs. For the 54 pair structure, Mo/Si ML structure's reflectance at 13.5-nm wavelength is 71.65% and the peak reflectance is up to 72.91% at 13.61 nm with a FWHM of 0.710 nm. Considering the practical process and using ruthenium and boron carbide as barrier layers at every interface with $d_{\mathrm{Ru}} = 1.4$ nm, $d_{\mathrm{B_4C}} = 0.2$ nm, $d_{\mathrm{Mo}} = 1.9$ nm, and $d_{\mathrm{Si}} = 3.5$ nm, we could achieve a higher reflectance 72.62% at 13.5-nm wavelength and peak reflectance 73.30% at 13.58 nm with Ru/Mo/B_4C/Si ML structure and a FWHM of 0.828 nm. Although the higher reflectance from simulation results seems to be 1.9-nm-thick Ru capping layer, we still chose a 2.0-nm Ru capping thickness for considering practical process. Finally, we have a multilayer structure with $d_{\mathrm{Ru}} = 1.4$ nm, $d_{\mathrm{B_4C}} = 0.2$ nm, $d_{\mathrm{Mo}} = 1.9$ nm, and $d_{\mathrm{Si}} = 3.5$ nm with 2.0-nm Ru as a capping layer to achieve a better reflectance 73.86% at 13.5-nm wavelength, a peak reflectance 74.42% at 13.57 nm, and a FWHM of 0.845 nm. By inserting two kinds of materials as barrier layers (i.e., ruthenium and boron carbide) to the Mo/Si ML structure and Ru as the capping layer, a high-performance interface-engineered Ru/Mo/B_4C/Si ML structure was designed at 13.5-nm wavelength. The reflectance has been improved and the thermal stability is expected to be improved in a pratical lithography system as well.

In the future, the fabrication process and the complete EUVL mask (mutilayer, absorber layer, and anti-reflective coating layer) should be studied.

Bibliography

[1] W. W. Gibbs, "Gordon E. Moore-Part 2," *Scientific American*, 1997.

[2] Lithography in international technology roadmap for semiconductor, 2010.

[3] B. Wu and A. Kumar, "Extreme ultraviolet lithography: A review," *J. Vac. Sci. Technol.*, vol. 25, 2007.

[4] O. Wood, C-S. Koay, K. Petrillo, "Integration of EUV lithography in the fabrication of 22-nm node devices," *Proc. SPIE*, vol. 7271, no. 727104, pp. 1-9, 2009.

[5] K-B. Kim, "A novel technique for projection-type electron-beam lithography," *SPIE Newsroom*, 2008, http://spie.org/x31901.xml?ArticleID=x31901.

[6] D. Sweeney, "Extreme ultraviolet lithography: Imaging and Future," *EUVL Progress Report*, https://www.llnl.gov/str/Sween.html.

[7] H. Kinoshita, T. Kaneko, H. Takei, N. Takeuchi, and S. Ishhara, "Study on x-ray reduction projection lithography," presented at the 47th Autumn Meeting of the *Jpn. Soc. of Appl. Phys.*, pp. 28-ZF-15, 1986.

[8] T. Namioka, "Current research activities in the field of multilayers for soft x-rays in Japan," *Revue Phys. Appl.*, vol. 23, pp. 1711-1726, 1988.

[9] W. T. Silfvast and O. R. Wood II, "Tenth micron lithography with a 10 Hz 37.2 nm sodium laser," *Microelectron. Eng.*,vol. 8, pp. 3-11, 1988.

[10] A. M. Hawryluk and L. G. Seppala, "Soft x-ray projection lithography using an x-ray reduction camera," *J. Vac. Sci. Technol.*, vol. 6 (B), pp. 2162-2166, 1988.

[11] D. A. Tichenor, et al., "10x reduction imaging at 13.4nm," *OSA Proc.*, vol. 23, pp. 89-97, 1994.

[12] H. Mizuno, G. McIntyre, C-S Koay, M. Burkhardt, B. La Fontaine, and O. Wood, Proc,“ Flare evaluation of ASML alpha demo tool,” *Proc. SPIE*, vol.7271, 72710U, 2009.

[13] P. J. Silverman, “Extreme ultraviolet lithography: overview and development status,” *SPIE*, vol. 4, pp. 011006-011010, 2005.

[14] K. Uchikawa, S. Takahashi, N. Kagtakura, T. Oshino, S. Kawata, and T. Yamaguchi, “Pattern displacement measurements for Si stencil reticles,” *J. Vac. Sci. Technol.*, vol. 17 (B), pp. 2868–2872 , 1999.

[15] S. D. Berger and J. M. Gibson, “New approach to projection-electron lithography with demonstrated 0.1 micron linewidth,” *Appl. Phys. Lett.*, vol. 57, pp. 153–155, 1990.

[16] D. A. Tichenor, A. K. Ray-Chaudhuri, W. C. Replogle, R. H. Stulen, G. D. Kubiak, P. D. Rockett, L. E. Klebanoff, K. L. Jefferson, A. H. Leung, J. B. Wronsky, L. C. Hale, H. N. Chapman, J. S. Taylor, J. A. Folta, C. Montcalm, R. Soufli, E. Spiller, K. Blaedel, G. E. Sommergren, D. W. Sweeney, P. Naulleau, K. A. Goldberg, E. M. Gullikson, J. Bokor, P. J. Batson, D. T. Attwood, K. H. Jackson, S. D. Hector, C. W. Gwynn, and P. Yan, “System integration and performance of the EUV engineering test stand,” *Proc. SPIE*, vol. 4343, pp. 19–37, 2001.

[17] A. Barty, P. B. Mirkarimi, D. G. Stearns, et al., “EUVL mask blank repair,” *Proc. SPIE*, vol. 4688, pp. 385–394, 2002.

[18] P-Y. Yan, G. Zhang, A. Ma, and T. Liang, “TaN EUVL mask fabrication and characterization,” *Proc. SPIE*, vol. 4343, pp. 409–414, 2001.

[19] P-Y. Yan, “The impact of EUVL mask buffer and absorber material properties on mask quality and performance,” *Proc. SPIE*, vol. 4688, pp. 150–160, 2002.

[20] J. R. Wasson, S-I. Han, N. V. Edwards, E. Weisbrod, W. J. Dauksher, and P. J. S. Mangat, “Integration of Anti-reflection Coatings on EUV Absorber Stacks,” *Proc. SPIE*, vol. 4889, pp. 382-388, 2002.

[21] S-Y. Lee, T-G. Kim, C-Y. Kim, I-Y. Kang, Y-C. Chung, and J. Ahn "Combined absorber stack for optimization of the EUVL mask," *Proc. SPIE*, vol. 6151, pp. 61511Y, 2006.

[22] D. He and F. Cerrina, "Process dependence of roughness in a positive-tone chemically amplified resist," *J. Vac. Sci. Technol.*, vol. 16 (B), pp. 3748–3751, 1998.

[23] H-B. Cao, Y. Wang, B. J. Rice, et al., "Sources of line-width roughness for EUV resists," *Proc. SPIE*, vol. 5376, pp. 757–764, 2004.

[24] E. Spiller, "Soft X-Ray Optics," *SPIE Optical Engineering Press*, ch. 8, 1994.

[25] K. M. Skulina, C. S. Alford, R. M. Bionta, D. M. Makowiecki, E. M. Gullikson, R. Soufli, J. B. Kortright, and J. H. Underwood, "Molybdenum/beryllium multilayer mirrors for normal incidence in the extreme ultraviolet," *Appl. Opt.*, vol. 34, pp. 3727-3730 , 1995.

[26] D. G. Stearns, R. S. Rosen, and S. P. Vernon, "Multilayer mirror technology for soft-X-ray projection lithography," *Appl. Opt.*, vol. 32, pp. 6952-6960, 1993.

[27] C. C. Lee, "Thin Film Optics and Coating Technology," *Yi Hsien Publishing Co.*, 5^{th} Ed., 2006.

[28] H. M. Liddell and H. G. Jerrard, "Computer aided techniques for the design of multilayer filters," *Taylor & Francis*, 1^{st} edition, 1981.

[29] A.V. Vinogradov and B. Y. Zeldovich, "X-ray and far UV multilayer mirrors: principles and possibilities," *Appl. Opt.*, vol. 16, 89-93, 1977.

[30] F. Schäers, "Multilayers for the EUV/soft x-ray range," *Physica B*, vol. 283, pp. 119-124, 2000.

[31] E. Louis, E. Zoethout, R. W. E. van de Kruijs, et al., "Multilayer coatings for the EUVL process development tool," *Proc. SPIE*, vol. 5751, pp. 1170–1177, 2005.

[32] R. Soufli and E. M. Gullikson, "Reflectance measurements on clean surfaces for the determination of optical constants of silicon in the extreme ultravioletsoft- x-ray region," *Appl. Opt.*, vol. 36, pp. 5499–5507, 1997.

[33] R. Soufli and E. M. Gullikson, "Absolute photoabsorption measurements of molybdenum in the range 60 to 930 eV for optical constant determination," *Appl. Opt.*, vol. 37, pp. 1713–1719, 1998.

[34] C. Tarrio, R. N. Watts, T. B. Lucatorto, J. M. Slaughter, and C. M. Falco, "Optical constants of in situ-deposited films of important extreme-ultraviolet multilayer mirror materials," *Appl. Opt.*, vol. 37, pp. 4100–4104, 1998.

[35] U. Schlegel, "Determination of the optical constants of Ruthenium in the EUV and soft x-ray region using synchrotron radiation," *Diploma thesis*, Technische Fachhochschule Berlin, 2000.

[36] B. L. Henke, E. M. Gullikson, and J. C. Davis, "X-ray interactions: photoabsorption, scattering, transmission, and reflection at $E = 50 - 30,000$ eV, $Z = 1 - 92$," *At. Data Nucl.* Data Tables, vol. 54, pp. 181–342, 1993. The updated version of these data is available at http://henke.lbl.gov/optical_constants/asf

[37] X-Ray and Gamma-Ray Data, http://physics.nist.gov/PhysRefData/contentsxray.html.

[38] Elastic Photon-Atom Scattering, http://physci.llnl.gov/Research/scattering/.

[39] M. Malinowski, C. Steinhaus, M. Clift, L.E. Klebanoff, S. Mrowka, R. Soufli, "Controlling contamination in Mo/Si multilayer mirrors by Si surface-capping modifications," *Proc. SPIE*, vol. 4688, pp. 442–453, 2002.

[40] M. Malinowski, "EUV optics contamination control gas blend carbon mitigation data and final report," *International SEMATECH*, Project LITH 113, Agreement 399509-OJ.

[41] S. Graham, C. Steinhaus, M. Clift, and L. Klebanoff, "Radio-frequency discharge cleaning of silicon-capped Mo/Si multilayer extreme ultraviolet optics," *J. Vac. Sci. Technol.*, vol. 20 (B), pp. 2393–2400, 2002.

[42] S. Bajt, J. B. Alameda, T. W. Barbee Jr., W. M. Clift, J. A. Folta, B. Kaufmann, E. A. Spiller, "Improved reflectance and stability of Mo/Si multilayers," *Opt. Eng.*, vol. 41, pp. 1797–1804, 2002.

[43] S. Bajt, Z. R. Dai, E. J. Nelson, M. A. Wall, J. B. Alameda, N. Q. Nguyen, S. L. Baker, J. C. Robinson, J. S. Taylor, A. Aquila, N. V. Edwards, "Oxidation resistance and microstructure of ruthenium-capped extreme ultraviolet lithography multilayers," *J. Microlith., Microfab., Microsyst.*, vol. 5 (2), pp. 023004-1-023004-13, 2006.

[44] S. Bajt, S. Hau-Riege, J. Alameda, F. Dollar, M. Chandhok, M. Fang, "Protective capping layer for EUVL optics using TiO_2," *4^{th} International Extreme Ultraviolet Lithography Symposium*, 2005.

[45] A. K. Petford-Long, M. B. Stearns, C.-H. Chang, S. R. Nutt, D. G. Stearns, N. M. Ceglio, and A. M. Hawryluk, "High-resolution electron microscopy study of x-ray multilayer structures," *J. Appl. Phys.*, vol. 61, p.p. 1422–1428, 1987.

[46] K. Holloway, K. Ba Do, and R. Sinclair, "Interfacial reactions on annealing molybdenum-silicon multilayers," *J. Appl. Phys.*, vol. 65, p.p. 474– 480, 1989.

[47] S. Yulin, T. Feigl, T. Kuhlmann, N. Kaiser, A. I. Fedorenko, V. V. Kondratenko, O. V. Poltseva, V. A. Sevryukova, A. Y. Zolotaryov and E. N. Zubarev, "Interlayer transition zones in Mo/Si superlattices," *J. Appl. Phys.*, vol. 92, p.p. 1216-1220, 2002.

[48] S. Braun, H. Mai, M. Moss, R. Scholz, and A. Leson, "Mo/Si multilayers with different barrier layers for applications as extreme ultraviolet mirrors," *Jpn. J. Appl. Phys.*, vol. 41, p.p. 4074-4081, 2002.

[49] I. Nedelcu, R. W. E. van de Kruijs, A. E. Yakshin, and F. Bijkerk, "Microstructure of Mo/Si multilayers with boroncarbide diffusion barrier layers," Appl. Opt., vol. 48, p.p. 155-160, 2009.

[50] M. G. Pelizzo, M. Suman, G. Monaco, P. Nicolosi, and D. L. Windt, "High performance EUV multilayer structures insensitive to capping layer optical parameters," Opt. Exp., vol. 16, p.p. 15228-15237, 2008.

[51] S. Bajta, N. V. Edwardsb, T. E. Madeyc, "Properties of ultrathin films appropriate for optics capping layers exposed to high energy photon irradiation," *Surf. Sci. Rep.*, vol. 63, p.p. 73–99, 2008.

[52] D. L. Windt, R. Hull, and W. K. Waskiewicz, "Interface imperfections in metal/Si multilayers," *J. Appl. Phys.*, vol. 71, p.p. 2675–2678, 1992.

[53] T. E. Madey, N. S. Faradzhev, B. V. Yakshinskiy, N. V. Edwards, "Surface phenomena related to mirror degradation in extreme ultraviolet (EUV) lithography," *Appl. Surf. Sci.*, vol. 253, p.p. 1691–1708, 2006.

[54] S. B. Hill, I. Ermanoski, C. Tarrio, T. B. Lucatorto, T. E. Madey, S. Bajt, M. Fang and M. Chandhok, "Critical parameters influencing the EUV-induced damage of Ru-capped multilayer mirrors," *Proc. SPIE*, vol. 6517, p.p. 65170G1-G12, 2007.

Vita

Fang-Yi Liu was born in Ping-Tung, Taiwan on April 27, 1987. She received the B.S. degree in the Department of Biomechatronic Engineering from National Chiayi University (NCYU) in June 2009. She entered the graduate program for Science and Technology of Accelerator Light Source, National Chiao Tung University (NCTU) in September 2009. She majors in thin-film optics and extreme ultra-violet lithography. She received the M.S. degree from NCTU in January 2012.